Tuning the bulk properties of bidisperse granular mixtures by size ratio

Nishant Kumar[a,*], Vanessa Magnanimo[a], Marco Ramaioli[b], Stefan Luding[a]

[a]*Multi Scale Mechanics (MSM), CTW, MESA+, University of Twente, P.O. Box 217, 7500 AE Enschede, The Netherlands.*
[b]*Chemical and Process Engineering, Faculty of Engineering and Physical Sciences (J2), University of Surrey, Guildford, Surrey, United Kingdom, GU2 7XH.*

Abstract

By using Discrete Element simulations, we study the bulk properties of bidisperse granular mixtures. We focus on the role of the size ratio between components and show that the effective bulk modulus of a granular (base) assembly can be enhanced by up to 20% by substituting as little as 5% of its volume with smaller radius particles. Using particles of a similar size barely affects the average bulk properties of the assembly. On the other extreme, when a huge number of very small particles are included, most of them lie in the voids of the base material, acting as rattlers, leading to an overall weakening effect. In between the limits, for dense systems, an optimum size ratio that maximizes the bulk modulus of the mixture can be found. Conversely, loose systems always get weaker since more and more small particles become rattlers. Finally, we relate the mixture properties with the 'typical' pore size in a disordered structure as induced by the combined effect of operating volume fraction and size ratio.

Keywords: DEM, granular, bidisperse mixtures, bulk modulus, polydispersity, fabric anisotropy

1. Introduction

Granular materials are widely used as raw materials or intermediate products in various industries, including pharmaceutical, mining, chemical, agricultural, household products and food industries. In many of these applications, processes involving milling, segregation, agglomeration, filtration and sieving are common and often lead to the generation of granular systems with large size ratios. Dealing with highly polydisperse systems is exceptionally challenging and often requires heuristic assumptions to be made, as prediction/control of the behavior is still an unsolved issue. A common and interesting class of polydisperse aggregates are bidisperse granular mixtures, where small particles (fines) are mixed with relatively bigger particles.

It is well known in the geomechanical community that the presence of fines strongly influences the mechanical behavior of granular soils. Scientific work on the topic is extensive and several studies have described the variation of elastic bulk stiffness and stress-strain behavior of

---

granular mixtures as a function of the volume of fines in the system (see [1, 12, 19, 25, 26, 31, 33] among others). Earlier work by Lade *et al.* [12] show that the the fines content in sand plays an important role in determining the sand structure and consequently affects the liquefaction potential of the sand. Vallejo [33] explains the strength of rock-sand mixtures based on the fine content and characteristic thresholds of the fines on the mixture porosity. Thevenayagam *et al.* [31] proposed the concept of intergranular void ratio (distinct from the measured, apparent void ratio) as the driving quantity for the mixture behavior. Similar to Vallejo [33], they identify five regimes for the liquefaction potential of the sand-silt mixtures and relate it to the participation of particles in the transfer of contact forces. Some studies [1, 19, 25] analyzed the contribution of fines to the effective void ratio, relative density as well as on the mechanical behavior of the mixed soil including instability, critical state, strength and stress dilatancy relations and confirm that it is not the same as that of the host coarse material. The small-strain mechanical stiffness of a mixture is also effected by the fines content, as e.g. shown by Salgado *et al.* [26] by using triaxial apparatus with bender elements. However, a better understanding of granular mixtures from a micromechanical perspective is needed, which experimentally is difficult to achieve for very small particles [5].

The problem has been recently approached also numerically [2, 16, 17, 20, 34, 35], by using the Discrete Element Method (DEM). Refs. [2, 16, 29, 35] confirm by means of simulations that even a small fine content can alter the mechanical response of sand-silt mixtures. The mechanical behavior of the soil is dominated by the network of coarse grains, whereas most part of the fine grains are in the voids surrounded by coarse grains and provide addition strength to the mixture. Recent works by Ueda *et al.* [32] explore the ranges of size and volume ratios of bidisperse granular mixtures to evaluate the shear strength in the quasi static regime. Minh *et al.* [17] address the bimodal nature of the strong/weak force network [24] in a granular mixture and its evolution under uniaxial compression varying the fine content in the system. Shire *et al.* [29] use a similar approach based on the idea of a stress transmitting fabric to assess the internal stability of idealized gap-graded soils. Shaebani *et al.* [27] used a mean field approximation and found a direct relation between the mean packing properties (components of classical stiffness matrix) in the case of (uniformly distributed) polydisperse aggregates. The micro-macro scaling is realized through a combination of moments of the particle size distribution. Ogarko and Luding [20, 21] found numerically that any polydispersity can be replaced by an equivalent bidisperse/tridisperse mixture when the first three/five size distribution moments are matched, excluding rattlers, in the case of isotropic compression in the collisional/dense regime.

However, all cited works refer to either systems with a homogeneous size distribution or to bidisperse mixtures of constant size ratio, where the relative volume of particles is varied. To the best of our knowledge, no systematic study has been done looking at the effects of varying the size of a very small volume of fines from a micromechanical perspective. The interest of our approach arises from geophysical hazards, like earthquakes, where the material volume remains constant, but the size of few particles can decrease quickly due to breakage. The change in the size distribution, even limited to a very small volume ratio, have been shown to play an important role in soil stability [1, 19, 25]. Important applications exist also in pharmaceutical and food processes such as chromatographic separation or extraction, where the flow though a deformable granular material depends strongly on the effective bulk modulus [23]. The development of bio-fuels based on algae relies also on effective de-watering which depends strongly on the bulk material compressibility [28]. In these industrial processes the focus is optimizing the performance of a given (granular) material with minimum modification, minimum costs [18]. Hence, the presence of small particles in a granular mass, which is often associated with weakness, is

here an asset for functionality. Other obvious applications this study covers building mixtures like concrete or asphalt, and shock absorbing materials.

We use DEM to study the effect on micro and macroscopic quantities of a monodisperse granular assembly by substituting only 5/105=4.76% of its volume with particles of different size (and same characteristics), thus generating a bidisperse mixture, with the main focus on the bulk modulus. We analyze the properties of the granular mixture on two phase spaces: (i) by varying the size ratio of fines to coarse and (ii) by spanning a wide range of volume fraction, and find the optimum size ratio that maximizes the bulk modulus at each volume fraction.

This paper is organized as follows: The simulation method and parameters used and the averaging definitions for scalar and tensorial quantities are given in section 2. The preparation test procedure for creating the granular mixture is explained in section 3. Section 4 is devoted to the rattlers (that do not contribute to the mechanical stabilities), and the effect of the size of fines on microscopic quantities like the coordination number. In section 5, we discuss the effect of the size of fines on macroscopic quantities like pressure and the jamming volume fraction. The effect of the size of fines on the contact network, quantified by the isotropic fabric, is also discussed there. Finally, section 6 is devoted to the bulk modulus and its variation with the size of fines for different volume fractions.

2. Numerical simulation and Material properties

In this section, the procedure of creating the granular mixture is presented. Later, we discuss the contact model and the simulation parameters.

The reference sample consists of $N_A^0 = 1050$ monodisperse particles A with radius $r_A = 1.5[mm]$. Starting from this base sample, many mixtures are created by substituting a given number of $\left(N_A^0 - N_A^T\right) = 50$ particles, with particles of species B of different radius $r_B \leq r_A$, such that the same volume $\left(N_A^0 - N_A^T\right)(4\pi/3)\, r_A^3 = N_B^T\,(4\pi/3)\, r_B^3 = V_B^T$ of material A is replaced by B [1]. The volume ratio of the two components in the final mixture is thus:

$$\Phi = \frac{V_B^T}{V_A^T} = \frac{\left(N_A^0 - N_A^T\right)}{N_A^T} = 5\% = \frac{N_B^T}{N_A^T}\left(\frac{r_B}{r_A}\right)^3, \tag{1}$$

and is much smaller than the pore space of the base material. The size ratio is varied systematically from the base case $r_B/r_A = 1$ down to $r_B/r_A = 0.13$; the number of B particles N_B varies together with r_B, while the volume ratio Φ is kept constant, as well as the volume of the individual species [2]. The total volume of particles is $V_T = V_A^T + V_B^T = 1.05 V_A^T$, so that volume of the box

---

[1]We want to point out here that the bidisperse systems found in the nature are not true bidisperse. Species have some polydispersity on top of their respective monodisperse sizes, even though small. One should add some polydispersity to each component to simulate realistic bidisperse mixtures. However, in a monodisperse sample adding a small polydispersity (less than 10%) has a negligible effect [20, 21] on the macroscopic properties like pressure (if the system remains amorphous which is the case in present work and we never reach crystalline states). Therefore, in this work, we limit ourself to true bidisperse mixtures to simplify the problem and for relatively easier data analysis and better understanding of scaling laws.

[2]We investigate the variation of particle radii down to $r_B/r_A = 0.13$. In general, such a material is assumed to be (e.g. in geomechanics) not filter stable anymore [4]. For $r_B/r_A < 0.20$, we see flattening in many measured macroscopic quantities, e.g. bulk modulus, for loose states, whereas in the denser systems, due to decrease in pore size, fines contribute, though these densities are difficult to achieve in realistic systems, with hard particles. We use the simulations also to explore regions of extreme size ratio for completeness. If frictionless and cohesionless fines would be used in gravity, they indeed would percolate and disappear. However, real fines might just stick enough to remain in the pores – if they are not flushed away by interstitial air- or fluid-flow.

V is same for different granular mixtures with different number of B particles N_B^T and at a given volume fraction $\nu = V_T/V$. Note that the substitution can be thought of addition when a system containing N_A^T particles of A is mixed with B with volume fraction $\Phi = 5\%$ of that of A.

In order to characterize the mixtures with different N_B^T, we define a dimensionless quantity β as:

$$\beta = \frac{N_B^T}{N_A^T + N_B^T}, \tag{2}$$

which is the ratio of small particles B to the total number of particle in the system. β is the input parameter of the simulation and is systematically varied to study its effect on the measured micro-macroscopic quantities.

For small β, few big particles B are present in the system, while for large β, many smaller particles B are present. The ratio of N_B^T to N_A^T in terms of β is given as

$$\frac{N_B^T}{N_A^T} = \frac{\beta}{1-\beta}, \tag{3}$$

and the size (radius) ratio is

$$\frac{r_B}{r_A} = \left(\Phi \frac{N_A^T}{N_B^T}\right)^{1/3} = \Phi^{1/3}\left(\frac{1-\beta}{\beta}\right)^{1/3}. \tag{4}$$

The sample made of only A particles is always used as reference case and corresponds to the case $r_B/r_A = 1$. It provides the minimum β, $\beta_{\min} = \Phi/(1+\Phi) = 0.05/1.05 = 0.0476$, and hence the minimum $N_B^T = \Phi N_A^T$. The variation of the radius ratio r_B/r_A is reported in Fig. 1(a) and shows a monotonic decrease with β [3].

The Discrete Element Method (DEM) [3] has been used extensively to study granular materials in biaxial and triaxial geometries under general deformation paths involving advanced contact models for fine powders [14, 30]. In this work, however, we restrict ourselves to the simplest isotropic deformation test and to the linear contact model without any friction between the particles [8, 11] [4].

This way we exclude all the non-linearities present in the system due to contact models and analyze the effect of size ratio on the bulk properties. Since DEM is a standard method, only the contact model parameters relevant for our simulation are briefly discussed.

The simplest linear normal contact force model when two particles i and j interact, at contact c, as shown in Fig. 1(b), is given as $\mathbf{f}_{ij}^n = f_{ij}^n \hat{\mathbf{n}} = (k\delta_c + \gamma\dot{\delta}_c)\hat{\mathbf{n}}$, where k is the contact spring stiffness, γ is the contact viscosity parameter, δ_c is the contact overlap and $\dot{\delta}_c$ is the relative velocity in the normal direction $\hat{\mathbf{n}}$. An artificial background dissipation force, $\mathbf{f}_b = -\gamma_b \mathbf{v}_i$, proportional to the velocity $\mathbf{v}_i$ of particle i is added (similarly of particle j), resembling the damping due to a

---

[3]Experimentally counting the number of particles of A and B of an existing packing is difficult and hence precisely measuring $\beta = N_B(N_A + N_B)$ is only convenient in DEM simulations or when a certain mixture is prepared manually from two species. Other parameters, that can be measured experimentally are the size ratio r_B/r_A or the relative mass/volume of the two species and their relation is given by Eq. (4). We use β as convenient input parameter to zoom into the most interesting results at $\beta \sim 0.4 - 0.7$. If the size ratio is used as parameter, the range of bigger variations in macroscopic quantities is squeezed to the left to $r_B/r_A \approx 0.2$, as can be seen in section 6, and Fig. 15.

[4]Isotropic deformation test means the deformation is isotropic in strain (volumetric). There are minor differences in the measured stresses in different eigen-directions and hence our packings are not strictly isotropic in stress (i.e., are not hydrostatic) [8].

Parameter	Symbol	Material A	Material B
Number of Particles	N^T	$N_A^T = 1000$	N_B^T varied [50–22500]
Radius	r	$r_A = 1.5$ mm	$r_B/r_A = \Phi^{1/3}\left(\frac{1-\beta}{\beta}\right)^{1/3}$
Particle density	ρ	$\rho_A = 2000$ [kg/m^3]	$\rho_B = \rho_A$ [kg/m^3]
Normal stiffness	k	$k_A = 5.10^8$ [N/m]	$k_B = k_A$
Normal Viscosity	γ	1 [Ns/m]	1 [Ns/m]
Background viscosity	γ_b	0.1 [Ns/m]	0.1 [Ns/m]

Table 1: Summary and numerical values of particle parameters used in the DEM simulations. β is the ratio of particles of B to the total number of particles, defined in Eq. (2). $\Phi = 0.05$ is the ratio of volume of B to that of A in the final mixture.

background medium, as e.g. a fluid [5]. Note that apart than the radius, materials A and B have the same interacting properties, i.e., stiffness, viscosity and density, see Table 1.

For a pair of particles i and j with masses m_i and m_j, a typical response time is the collision duration $t_c^{ij} = \pi/\sqrt{k/m_{ij} - (\gamma/2m_{ij})^2}$, where $m_{ij} = m_i m_j/(m_i + m_j)$ is the reduced mass [8]. In DEM, the integration time-step is chosen to be about 50 times smaller than the shortest time-scale $t_c = \min\left(t_c^{ij}\right)$ [14]. The parameters used in DEM simulations are presented in Table 1. For our system, material B sets the DEM time-step, as r_B and hence m_{BB} is smallest, leading to the smallest t_c^{BB}. The variation of t_c with β can be seen in Fig. 1(a). t_c decreases with increasing β, meaning that the smaller particles in the mixture lead to a reduction in the collision time and hence to a finer time-step. Due to computational limitations, the simulations were performed up to $\beta = 0.957$.

3. Preparation and test procedure

Each mixture, made of materials A and B as introduced in section 2 is created and further compressed using a unique, well defined protocol. The preparation consists of three parts: (i) randomization, (ii) isotropic compression, and (iii) relaxation, all equally important to achieve the initial mixtures for the following analysis. The initial configuration is such that spherical particles of particles A and B, are randomly generated in a 3D box without gravity, with low volume fraction and rather large random velocities, such that they have sufficient space and time to exchange places and to randomize themselves. This granular gas is then isotropically compressed, in order to approach a direction independent initial configuration with target volume fraction $\nu_0 = 0.64$, sightly below the jamming volume fraction, i.e., the transition point from

[5]We are interested in the macroscopic properties of static, stable and relaxed packings of jammed granular assemblies. A background dissipation γ_b is used for relaxing the particles faster which provides static, stable packings and saves computational time. If γ_b is small, the system needs longer time to relax, however, if γ_b is too large, the particles will not have enough time to find stable configurations and that are frozen rather quickly (overdamped). Therefore, the use of neither too weak nor too strong γ_b is recommended. We expect the chosen value of γ_b might have some local effects but should not have significant influence on the global macroscopic properties. In previous studies [6], this was tested by comparing different rates of compression, were no significant rate dependence was observed.

fluid-like behavior to solid-like behavior [6, 7, 9, 10, 22]. Recent studies show that for a given granular assembly, the jamming transition can be protocol (rate of deformation) dependent [7] and history dependent [9, 10], but this is beyond the scope of this study.

Isotropic compression is realized by a simultaneous inward movement of all the periodic boundaries of the system, with diagonal strain rate tensor $\dot{\mathbf{E}} = \dot{\epsilon}_v \left(-1, -1, -1\right)$, where $\dot{\epsilon}_v$ is the rate amplitude ($\dot{\epsilon}_v > 0$ in our convention represents compression) applied to the walls [6]. This is followed by a relaxation period at constant volume fraction to allow the particles to fully dissipate their energy and to achieve a static configuration in mechanical equilibrium, indicated by the drop in kinetic to potential energy ratio to almost zero. This relaxed state is further isotropically compressed until a target maximum volume fraction $\nu_{\max} = 0.82$ is achieved. The simulations are continued with negative rate amplitude in the unloading mode, until the initial $\nu_0 = 0.64$ is reached.

For each mixture, configurations at six different ν are picked from the unloading branch and relaxed, allowing to dissipate the kinetic energy and reach unjammed, non-overlapping stable packings [7]. As an example, we show in Fig. 2 isotropic samples with $\beta = N_B^T / \left(N_A^T + N_B^T \right) = 0.075$, 0.56, and 0.96 for loose and dense samples with volume fraction $\nu = 0.69$ and 0.82 respectively.

4. Microscopic Quantities

In this section, we present the general definitions of averaged microscopic parameters including the coordination number and the fraction of rattlers.

4.1. Mechanically stable system

In order to properly relate the macroscopic load, carried by the sample, with the active microscopic contact network, all particles that do not contribute to the force network are excluded from the analysis. In three dimensions, frictionless particles in absence of gravity with less than *four* contacts are thus 'rattlers', since they are not mechanically stable and hence do not participate to the force transmission [6, 8, 22]. The rattlers contacts are transient since the repulsive contact forces push them away from the mechanically stable backbone. Thus, if the packings were allowed to relax "forever", the rattlers would loose all of their contacts [6, 8]. From the snapshots in Fig. 2, where number of contacts of particle p is $C_p \geq 0$, all the particles with less than 4 contacts are removed. The rattlers exclusion is an iterative process until all remaining particles have at least 4 contacts ($C_p^* \geq 4$), that provides us a completely mechanically stable systems as shown in Fig. 3 (only particles B are shown).

Unless mentioned explicitly, we will denote N_A and N_B as the number of mechanically stable particles of A and B, respectively, and use them to compute micro- and macroscopic quantities. Any superscript 'T' relates to the total number of particles of A and B, including the rattlers.

---

[6]For the isotropic deformation tests, we move the (virtual) walls sinusoidally [10]. When there is a huge dispersity in the particle sizes ($r_A/r_B \gg 1$), some arching near the corners of the box can be seen in Fig. 3(f). We tried a different procedure deformation by moving all the grains according to an affine motion, but arching near the corners was still present. This is because the big sized A particles have less access to the corners (available box volume is small compared to the middle of the system), while smaller particles settle in the corners and support each other by providing 4 weak non-rattler contacts.

[7]Configurations from the unloading branch are more reliable since it is much less sensitive to the protocol and rate of deformation during preparation [6, 8].

4.2. Rattlers

In Fig. 4, we plot the number ratio of participating particles B with respect to A after removing the rattlers, i.e., N_B/N_A. For all cases, the assembly contains 95% by volume of big particles of A. Thus, N_A after removing rattlers is close to N_A^T, i.e., $N_A/N_A^T \approx 1$. With decreasing size of B, i.e., increasing β, an initial increase in the ratio N_B/N_A is seen, followed by a maximum and a later decrease for all the volume fractions. For small β, few B particles are present with size comparable to A. With increasing β and for all ν, the ratio N_B/N_A increases as more B particles of smaller size are introduced in the system while the number of A stays constant. For a fixed ν, there is an average void size created by A that can be most efficiently filled by an optimal (just fitting) B[8], the optimum size ratio r_B/r_A corresponds to a maximum in N_B/N_A. Indeed, when β increases further, meaning more smaller particles B in the system, the number of active (non-rattlers) particles B decreases, as most of them become rattlers, 'caged' in the voids of A [9]. This can be seen comparing Fig. 2(c) with Fig. 3(c). Therefore, the ratio N_B/N_A decreases after the maximum.

Another important observation is that with increasing ν, the maximum in N_B/N_A occurs at increasing β. This is because for increasing ν, the base assembly A is more compressed with smaller void size. That is smaller B particles already fill efficiently the voids of A as non-rattlers. For the densest case $\nu = 0.82$, the ratio N_B/N_A seems to saturate for large β. However when $\beta \rightarrow 1$, N_B will decrease and hence the ratio N_B/N_A. Due to the computational limitations, this observation can not be presented.

Fig. 4 also shows the ratio N_B/N_A including rattlers, same for all density represented by Eq. (3). N_B^T/N_A^T is higher than N_B/N_A, since N_B is smaller than N_B^T, while $N_A/N_A^T \approx 1$. Note that the dashed line is closer to the dense systems, where the majority of B particles are active particles.

4.3. Coordination number

The classical definition of coordination number is $C = M/N^T$, where M is the total number of contacts and N^T is the total number of particles [6, 8, 9]. In order to quantify the active contact network (excluding rattlers), we use the corrected coordination number: $C^* = M_4/N_4$, where M_4 is the total number of contacts of the N_4 particles with at least 4 contacts, i.e., $C_p^* \geq 4$ (see section 4.1). Note that, after excluding rattlers, the number of particles left in the system is $(N_A + N_B) = N_4 < N^T = (N_A^T + N_B^T)$

Fig. 5 shows the evolution of C^* with β for six different volume fractions. As expected, for a given composition (fixed β), the total coordination number of the system increases with volume fraction ν as the system becomes more dense and particles are both closer and better coordinated. For given density ν, C^* decreases continuously with β, since the number of non-rattler particles N_4 increases faster than the non-rattler contacts M_4; i.e., C^* decreases. At high β, an increase in C^* is seen, associated with the drop in active particles B, N_B, in other words N_B/N_A, as shown in Fig. 4 [9].

4.4. Dimensionless moments

The average radius and moments are among the fundamental quantities needed to characterize the particle size distribution [20]. Given $f(r)$ as the particle radii (size) distribution, $f(r)dr$ is the probability to find the radius between r and $r + dr$, with a normalization condition $\int_0^\infty f(r)dr = 1$ [6, 20]. For a bidisperse distribution $f(r) = f_A\Delta(r - r_A) + f_B\Delta(r - r_B)$, where $f_A = N_A/(N_A + N_B)$ and $f_B = N_B/(N_A + N_B)$ are the number fractions of A and B and $\Delta(r)$ is the Dirac-delta function. While $N^T = N_A^T + N_B^T$, without superscript (T denotes the total number of particles), $N_A + N_B = N_4$ is the total number of particles in the system with at least four contacts ($C_p^* \geq 4$, see section 4.1). The nth moment is $\langle r^n \rangle = \int_0^\infty r^n f(r)dr$. The mean particle radius for a bidisperse distribution is thus $\langle r \rangle = \int_0^\infty r f(r)dr = f_A r_A + f_B r_B$ and the nth moment is $\langle r^n \rangle = f_A r_A^n + f_B r_B^n$ with $f_A + f_B = 1$.

Fig. 6(a) shows the average radius of the system scaled with the radius of A; i.e., $\langle r \rangle / r_A$ excluding rattlers. Starting from 1, $\langle r \rangle / r_A$ decreases with increasing β due to the presence of smaller B particles [10]. This decrease is faster for higher ν and shows an inverse trend with respect to N_B/N_A in Fig. 4. For $\beta \to 1$, the size of B becomes very small compared to A so that they do not contribute, and the system excluding rattlers is mainly composed of A, so that $\langle r \rangle / r_A \to 1$.

The dimensionless moments of a polydisperse assembly O_1 and O_2 are defined as [20]:

$$O_1 = \frac{\langle r \rangle \langle r^2 \rangle}{\langle r^3 \rangle} \quad \text{and} \quad O_2 = \frac{\langle r^2 \rangle^3}{\langle r^3 \rangle^2}, \tag{5}$$

where it was shown that O_1 and O_2 are needed to completely quantify the fluid-like behavior of a granular assembly well below jamming. For our system, N_A and N_B change with β and volume fraction ν, hence O_1 and O_2 are different for different volume fractions. If the dimensionless moments O_1 and O_2 are known, the 2$^{\text{nd}}$ and 3$^{\text{rd}}$ dimensionless moments (moment scaled by $\langle r \rangle$) are:

$$\frac{\langle r^2 \rangle}{\langle r \rangle^2} = \frac{O_2}{O_1^2} \quad \text{and} \quad \frac{\langle r^3 \rangle}{\langle r \rangle^3} = \frac{O_2}{O_1^3}. \tag{6}$$

The nth moment is always greater or equal to the nth power of the mean radius, i.e., $\langle r^n \rangle / \langle r \rangle^n \geq 1$. Therefore, $O_1^2 \leq O_2$ and $O_1 \leq 1$, as also shown in Ref. [20]. For the full system including the rattlers,

$$\langle r \rangle^T = (1 - \beta)r_A + \beta r_B \quad \text{and} \quad \langle r^2 \rangle^T = (1 - \beta)r_A^2 + \beta r_B^2 \quad \text{and} \quad \langle r^3 \rangle^T = (1 - \beta)r_A^2 + \beta r_B^2. \tag{7}$$

Therefore, O_1 and O_2 for the full system become

$$O_1^T = \frac{[(1 - \beta) + \beta(r_B/r_A)][(1 - \beta) + \beta(r_B/r_A)^2]}{(1 - \beta) + \beta(r_B/r_A)^3} \quad \text{and} \quad O_2^T = \frac{[(1 - \beta) + \beta(r_B/r_A)^2]^3}{[(1 - \beta) + \beta(r_B/r_A)^3]^2}. \tag{8}$$

---

[8]Big particles A create voids filled by B. Different lattice arrangements of A provide the void size such that B touches A particles, giving the size ratio r_B/r_A for the most compact packing. A simple approach to measure this ratio for triangular, tetrahedron, square and cubic lattices formed by A particle is shown in appendix Appendix A).

[9]Note that the lowest limit of C^* in Fig. 5 is around 7, higher than the isostatic value of 6, in the frictionless case near the jamming transition. However, we do not present the datasets for even lower volume fractions since for $\beta \to 1$ and for smaller volume fraction the different mechanisms are active, e.g., very high relaxation time scales. Hence, the lowest volume fraction of $\nu = 0.691$ was chosen to analyze our datasets.

[10]This is understood from the inequality: $\langle r \rangle / r_A = f_A + f_B r_B/r_A = 1 - f_B + f_B r_B/r_A = 1 - f_B(1 - r_B/r_A) < 1$, since the second term is positive and smaller than unity.

Inserting the radius ratio $r_B/r_A = \Phi^{1/3}\left(\frac{1-\beta}{\beta}\right)^{1/3}$ from Eq. (4), where $\Phi = 0.05 = $ const. (see section 2), Eq. (8) can be re-written as

$$O_1^T = \frac{\left[(1-\beta)^{2/3} + \Phi^{1/3}\beta^{2/3}\right]\left[(1-\beta)^{1/3} + \Phi^{2/3}\beta^{1/3}\right]}{(1+\Phi)} \quad \text{and} \quad O_2^T = \frac{\left[(1-\beta)^{1/3} + \Phi^{2/3}\beta^{1/3}\right]^3}{(1+\Phi)^2}.$$
(9)

The asymptotic values for O_1^T and O_2^T when $\beta \to 1$ are $\Phi/(1+\Phi)$ and $\Phi^2/(1+\Phi)^2$, respectively. Fig. 6(b) and 6(c) show the evolution of O_1 and O_2 with β and ν. Both O_1 and O_2 are smaller than unity [20], decreasing with β, and show a similar trend as $\langle r \rangle/r_A$. The dashed lines in Fig. 6 represent the granular assembly including the rattlers, i.e., only a single line for all volume fractions.

4.5. Corrected volume fraction

It is interesting to look closer at the behavior of the corrected volume fraction ν^*, i.e., the volume fraction excluding the non-active particles

$$\nu^* = N_4 \frac{4\pi}{3} \frac{\langle r^3 \rangle}{V}.$$
(10)

Fig. 7(a) shows the corrected volume fraction ν^* versus β. For any volume fraction ν, ν^* decreases continuously with β, since the volume fraction of rattlers (mainly B) increases with β. For decreasing size of B, more and more B particles are 'caged' between the big particles A without having sufficient ($C_p^* \geq 4$) contacts [9]. For the reference case, when the radius of B is equal to that of A, (leftmost data points), $\nu^* \approx \nu$, and for the density close to the jamming point, $\nu^* \approx 0.98\nu$, as approximately 2% of the particles are rattlers, in agreement with the values reported in [9] for the monodisperse case.

For each mixture, we extract the jamming point ν_c, i.e., the volume fraction ν when the pressure p of the mixture (defined in section 5.2) approaches zero. Fig. 7(b) shows ν_c increasing with β and saturating for $\beta \to 1$. This can be understood since the number of non-rattler particles decreases with β, as also seen in Fig. 7(a), until they reach the number of N_A^T. Therefore, with increasing β, one needs to compress the system further (or increase the volume fraction) to make sure particles achieve an overlapping, jammed configuration, leading to increase in ν_c with β. For $\beta \to 1$ and volume fractions near ν_c, all particles B are rattlers and therefore ν_c saturates for $\beta \to 1$. Note that ν^* in Fig. 7(a) excludes the rattlers while ν_c in Fig. 7(b) includes the rattlers. The relation between ν_c and β can be fitted by the linear relation:

$$\nu_c = \nu_c^0 + (\nu_c^1 - \nu_c^0)\frac{\beta - \beta_{\min}}{1 - \beta_{\min}},$$
(11)

where $\nu_c^0 = 0.646$ for the monodisperse case for $\beta_{\min} = 0.05/1.05 = 0.0476$. $\nu_c^1 = 0.682$ is the only fit parameter for $\beta = 1$, obtained by fitting the simulation data in Fig. 7(b) up to $\beta = 0.8$. Note that the $\nu_c^0 = 0.646$ value measured from the simulation for the monodisperse case is consistent with results ν_c^0 in Ref. [9] for different system size. Assuming that for $\beta \to 1$ only A particles contribute to te structure, we estimate the saturation volume fraction as

$$\nu_c^2 = \nu_c^0 (1 + \Phi) = 0.678,$$
(12)

in consistent with the measured values for $\beta \to 1$ as shown in Fig. 7(b).

9

5. Macroscopic Quantities

231 In the previous section, we focused on the averaged microscopic quantities; rattlers and co-
232 ordination number. Next we focus on defining the averaged macroscopic quantities – stress and
233 fabric (structure), that reveal interesting bulk features and provide information about the state of
234 the packing via its response to applied deformation.

235 *5.1. Fabric*

From the DEM simulations, one can determine the fabric tensor in order to characterize the
geometry/structure of the static aggregate [6, 11], defined as

$$\mathbf{F}^T = \frac{1}{V} \sum_{p=1}^{N^T} V_p \sum_{c=1}^{C_p} \mathbf{n}^c \otimes \mathbf{n}^c, \tag{13}$$

where V_p is the volume of particle p, which lies inside the averaging system volume V, and $\mathbf{n}^c$ is
the normal unit branch vector pointing from center of particle p to contact c. C_p is the number
of contacts of particle p and N^T represents the total number particles. In the case of isotropically
compressed systems, the isotropic fabric F_v^T is the quantity of interest and is obtained by taking
the trace of Eq. (13) as:

$$F_v^T = \mathrm{tr}\left(\mathbf{F}^T\right) = \frac{1}{V} \sum_{p=1}^{N^T} V_p \sum_{c=1}^{C_p} 1 = \frac{1}{V} \sum_{p=1}^{N^T} V_p C_p. \tag{14}$$

Note that we exclude iteratively the rattlers from the system (see section 2), and observe that
their contribution to the fabric is small (as shown in Fig. 8). Therefore, the isotropic fabric for
non-rattler particles with stable non-rattler contacts ($C_p^* \geq 4$) is:

$$F_v = \frac{1}{V} \sum_{p=1}^{N_4} V_p C_p^* \approx \frac{1}{V} \sum_{p=1}^{N^T} V_p C_p, \tag{15}$$

236 where $N_4 = (N_A + N_B) \leq \left(N_A^T + N_B^T\right) = N^T$ is the total number of particles excluding the rattlers,
237 as defined in section 2.
238 Fig. 8 shows the evolution of F_v calculated using Eq. (15) with β for six volume fractions.
239 The first important observation if that the contribution of rattlers to the fabric is small and F_v^T is
240 very close to F_v. For a given mixture (fixed β), F_v increases with volume fraction v, meaning
241 that the system becomes more connected. On the other hand, for a given v, F_v first increases and
242 then decreases, The maximum of F_v is correlated with the average voids created by particles A,
243 that, for a given v and size of B can be optimally filled (see appendix Appendix A). The behavior
244 of F_v is similar to that of number of non-rattlers particles of B, N_B, observed in Fig. 4, since
245 $F_v \propto N_4$ (Eq. (15)).
We are interested in the relation of isotropic fabric with the system's mean packing properties
e.g. volume fraction, average coordination number. An expression relating isotropic fabric to
mean packing properties, similar to that given in Refs. [6, 9, 27], is:

$$F_v = g_3 v^* C^*, \tag{16}$$

where v^* and C^* are the volume fraction and mean corrected coordination number of the system respectively, excluding the rattlers, as defined in section 4.1, and g_3 is related to the moments of size distribution [11]. For a bidisperse size distribution, g_3 excluding the rattlers is given as (see appendix Appendix B for derivation):

$$g_3 := g_3^\chi = \frac{1}{\langle r^3 \rangle} \frac{r_A^3 \Omega_A^{-1} f_A + r_B^3 \Omega_B^{-1} f_B \chi}{\Omega_A^{-1} f_A + \Omega_B^{-1} f_B \chi} = \frac{\langle r^3 \rangle_g}{\langle r^3 \rangle}, \tag{17}$$

where r_A and r_B are the radii of A and B with number fraction f_A and f_B respectively. $\Omega(r) = 2\pi \left[1 - \sqrt{1 - \langle r \rangle^2 / (r + \langle r \rangle)^2} \right]$ is the space angle covered on a particle of radius r by neighboring particles of radius $\langle r \rangle$. χ is the ratio of the linear compacity (or the total fraction of shielded surface which is proportional to product of space angle and number of non-rattler contacts, defined in appendix Appendix B) of B to A. The unknown in the functional form of Eq. (17) is χ, the ratio of the linear compacities of B to A (see appendix Appendix B). Fig. 9(a) shows the evolution of the measured ratio χ with the size ratio r_A/r_B, as extracted from simulations for different volume fractions. χ increases with increasing size ratio and is dependent on the volume fraction v, in agreement with Ref. [6, 27]. For fitting the data in Fig. 9(a), we propose

$$\chi = 1 + \frac{1}{2} \left(\frac{1}{\Lambda} - 1 \right) \left[1 + \mathrm{erf} \left(a(v) \left(\frac{r_A}{r_B} - b(v) \right) \right) \right], \tag{18}$$

where erf(...) is the error function and $a(v) = 0.25 \, (v/v_c)^4$ and $b(v) = 4.5 + a(v)$ are empirical relations. $1/\Lambda \approx 1/0.4$ is the maximum compacity ratio $\max(\chi) = 1/\Lambda$ and is reached near the jamming transition (see appendix Appendix B for the bounds of linear compacity) [12].

The measured g_3^χ using Eq. (17) is plotted in Fig. 9(b). g_3^χ is greater than 1 for all volume fraction, increasing with β to a maximum followed by a decrease, similar as N_B/N_A shown in Fig. 4. g_3 measured assuming constant linear compacity [6, 15, 27], i.e., g_3^1 with $\chi = 1$ is also plotted in Fig. 9(b) shows similar trend as g_3^χ and is higher. Asymptotic analysis for $\beta \to 1$, considering all the particles present in the system and with constant linear compacity tells us that g_3^T diverges as $(1 - \beta)^{-2/3}$, in agreement with the behavior shown in Fig. 9(b).

Fig. 10(a) shows the relation of F_v with the mean packing properties via g_3 using Eq. (16), and a good agreement is observed with small errors up to 5% for the highest densities and $\beta \to 1$. Modification of the linear compacity helps to improve the relation of F_v with the mean packing properties, while a constant linear compacity assumption works only for low v and up to intermediate β, as seen in Fig. 10(b). For dense states and high β, the constant linear compacity assumption can lead to up to 45% error in the prediction of F_v. This is due to the fact that very small B particles are present in large numbers, participating in the contact network, so that the assumption of the linear compacity independent with particle radii, is not valid anymore. The better understanding of the linear compacity that can account for large numbers of very small particles in highly polydisperse systems is subject of a future study. Finally, we attribute the poor agreement between F_v^T and $g_3^1 v C$ as used in Ref. [6, 8, 27], as shown in Fig. 10(c), to the fact that homogeneous size distributions were used, not excluding one of the species strongly from the contact network.

---

[11] Refs. [6, 9, 27] used the corrected coordination number $C = M_4/N$ in Eq. (16), while is different than $C^* = M_4/N_4$ used in this study. It was checked that using C in Eq. (16) instead of C^* worsen the comparison with F_v.

[12] The bounds of compacity and hence χ are presented in appendix Appendix B. Due to these bounds, we fit the DEM data using an error function, which is an empirical choice (also a tangent hyperbolic could be used).

5.2. Pressure

Besides the fabric, one can determine the static stress tensor as

$$\boldsymbol{\sigma} = \frac{1}{V} \sum_{c=1}^{M} \mathbf{l}^c \otimes \mathbf{f}^c, \qquad (19)$$

which is the sum of the dyadic products between the branch vector $\mathbf{l}^c = l_c \mathbf{n}^c$ and the contact force $\mathbf{f}^c = k\delta_c \mathbf{n}^c$ over all the contacts (an exemplary two particle contact is shown in Fig. 1(b)) in the system volume V, where the contribution of the kinetic energy has been neglected [8, 13]. The isotropic component of the stress is the pressure $P = \text{tr}(\boldsymbol{\sigma})/3$. The non-dimensional pressure is defined as:

$$p_n = \frac{2\langle r_A \rangle}{3k} \text{tr}(\boldsymbol{\sigma}) = \frac{2\langle r_A \rangle}{k} P, \qquad (20)$$

scaled by constant $2\langle r_A \rangle / k$. In bi-axial experiments, the pressure P can be measured, and hence p_n can be estimated. Note that p_n is used in the following to avoid dimensions of pressure. The size sensitive non-dimensional pressure is defined as [6, 8, 9]:

$$p = \frac{2\langle r \rangle}{3k} \text{tr}(\boldsymbol{\sigma}) = \frac{2\langle r \rangle}{k} P. \qquad (21)$$

Note that in this work, the pressure calculated considering M_4 non-rattler contacts is very close to the one from M contacts, as $M - M_4$ are temporary, very weak (rattler) contacts that barely contribute to the average stress.

Fig. 11(a) shows the evolution of the non-dimensional pressure p_n with β for six different volume fractions ν as shown in the legend. For a given β, p_n increases with ν as the particles are more compressed [8]. On the other hand, for a given density, p_n systematically decreases with β. This observation is linked to the behavior of the corrected volume fractions ν^* (section 4.5), as seen in Fig. 7(a), which also decrease systematically with β. For moderate and large β, most of the contribution to pressure comes from particles A, while the contribution of B is negligible, as both overlap and radius are small and hence is their stress (proportional to both) becoming negligible for large β (data not shown). Fig. 11(b) shows the evolution of the non-dimensional pressure p using Eq. (21) [8]. For the smallest β, where the system is composed of only A particles p_n and p are the same. For fixed ν, p decreases much faster than p_n with β, since p is a product of p_n and $\langle r \rangle$, both decreasing with β. In this case, the behavior of p differs from F_v, see Fig. 8. Another important observation is that the behavior of p has a similar trend as C^* in Fig. 5. For a given mixture (fixed β), F_v increases with volume fraction ν, as do both coordination number and pressure,

We try to better understand the evolution of the non-dimensional pressure by looking at the individual components that contribute to Eq. (19). Due to the linear contact model used without any tangential component, the force and the branch vectors are parallel for all contacts (see Fig.

12

1(b)). Hence, Eq. (21) becomes [6, 27]:

$$
\begin{aligned}
p &= \frac{2\langle r \rangle}{3k}\mathrm{tr}(\boldsymbol{\sigma}) \approx \frac{2\langle r \rangle}{3k}\frac{1}{V}\mathrm{tr}\left(\sum_{c=1}^{M_4}\mathbf{l}^c \otimes \mathbf{f}^c\right) = \frac{2\langle r \rangle}{3V}\sum_{c=1}^{M_4}\mathrm{tr}\left(l_c\mathbf{n}^c \otimes \delta_c\mathbf{n}^c\right) \\
&= \frac{2\langle r \rangle}{3V}\sum_{c=1}^{M_4}\left[\langle l_c \rangle + l_c'\right]\left[\langle \delta_c \rangle + \delta_c'\right]\underbrace{\mathrm{tr}\left(\mathbf{n}^c \otimes \mathbf{n}^c\right)}_{=1} = \frac{2\langle r \rangle}{3V}M_4\left[\langle l_c\rangle\langle\delta_c\rangle + \langle l_c'\delta_c'\rangle\right] \\
&= \frac{2\langle r \rangle}{3V}M_4\left[\langle l_c\rangle\langle\delta_c\rangle + \langle l_c'\delta_c'\rangle\right]\left[\frac{\nu^*}{(4\pi/3)N_4\langle r^3\rangle/V}\right] \\
&= \frac{C^*\nu^*}{2\pi}\frac{\langle r \rangle}{\langle r^3\rangle}\left[\langle l_c\rangle\langle\delta_c\rangle + \langle l_c'\delta_c'\rangle\right],
\end{aligned}
\tag{22}
$$

where the rattlers offer no contribution and the prime $'$ represents the fluctuations with respect to the average. The first term in Eq. (22) considers the average overlap $\langle\delta_c\rangle$ and the average branch vector $\langle l_c\rangle$. The second term is the contribution due to the correlated fluctuations in branch vector and overlap.

Fig. 11(c) shows the evolution of the first term $\langle r\rangle\langle l_c\rangle\langle\delta_c\rangle/\langle r^3\rangle$ in Eq. (22). For a given β with increasing ν, the average overlap $\langle\delta_c\rangle$ increases [9], $\langle l_c\rangle$ slightly decreases and $\langle r\rangle/\langle r^3\rangle$ increases. Therefore $\langle r\rangle\langle l_c\rangle\langle\delta_c\rangle/\langle r^3\rangle$ increases with ν (for fixed β) and decreases with β (for fixed ν), as seen in Fig. 11(c), except for very high ν's and β's. The fluctuation factor $\langle r\rangle\langle l_c'\delta'\rangle/\langle r^3\rangle$ increases with both ν and β, as seen in Fig. 11(d). The common term C^* has a similar trend as of $\langle r\rangle\langle l_c\rangle\langle\delta_c\rangle/\langle r^3\rangle$, as seen in Fig. 5. Comparing Fig. 11(c) and Fig. 11(d), we conclude that the decrease in p with β observed in Fig. 11(a) is mainly associated with the decrease of both $\langle r\rangle\langle l_c\rangle\langle\delta_c\rangle/\langle r^3\rangle$ and C^*, while the fluctuation term is very small.

The non-dimensional pressure p can be written in the same form as given in Ref. [6]:

$$
p = p_0\frac{\nu^*C^*}{\nu_c}(-\varepsilon_{\mathrm{v}})\left[1 - \gamma_p(-\varepsilon_{\mathrm{v}})\right]
\tag{23}
$$

where the quantity $(-\varepsilon_{\mathrm{v}})$ is the true or logarithmic volume change of the system proportional to the ratio of average overlap to the mean radius $\langle\delta_c\rangle/\langle r\rangle$ (see Appendix C). $p_0 \approx 0.043$ for uniform size distributions [6, 8]; though small variation in measured p_0 is reported for different deformation paths [9, 10] however, p_0 is not constant for an arbitrary wide bidisperse size distributions, as the case in this work, as shown in Fig. 12(a) (see Appendix C for more details about calculating p_0). Fig. 11(b) shows the prediction for the non-dimensional pressure p using Eq. (23) without the second small term. Since, γ_p is positive, the pressure is slightly over predicted, mainly in the dense regime and for the monodisperse case. Finally, Fig. 12(b) shows a perfect prediction of the measured pressure p when compared with Eq. (23), again without the non-linear term. Only for highly dense cases, a maximum error of few percent can be seen, which could be avoided by including the non-linearity with γ_p.

As final stage, we want to study how the bulk modulus of the granular assembly varies with the contribution of the fines.

6. Bulk modulus

For each granular mixture, we calculate the bulk modulus by first relaxing (see section 3) and then applying an incremental pure volumetric perturbation of small amplitude to the sample (the

13

volume fraction of the system is changed by isotropically moving all the walls by $dv \approx 0.00015$) [11]. The bulk modulus is then the ratio between the measured change in pressure and the applied strain dv/v, small enough to prevent irreversible contact rearrangements [11]:

$$K' = v\frac{dP}{dv}. \tag{24}$$

The non-dimensional bulk modulus is thus [6, 11]:

$$K = \frac{2\langle r_A \rangle}{k} v\frac{dP}{dv}, \tag{25}$$

where $2\langle r_A \rangle$ is the average particle radius of A which provides the backbone to the granular assembly and k is the particle stiffness. Just like the pressure P, the bulk modulus K' can be estimated in the bi-axial experiments, and hence K can be calculated. Note that measuring non-dimensional bulk modulus K measured using Eq. (25) is not the same if non-dimensional pressure p was used, i.e., $K \neq v\frac{dp}{dv}$.

Fig. 13(a) shows the evolution of the bulk modulus K plotted against β for different volume fractions v. As expected, K increases systematically with density v. For loose states ($v = 0.69$, 0.72), K mostly decreases with increasing β to the limit case $\beta \rightarrow 1$, as discussed below. The behavior associated with denser states is much more interesting, as we observe an increase in K to a maximum, followed by a decrease for larger β. Note that the value of β where K becomes maximum increases with increasing densities and the maximum also becomes stronger. From Fig. 13(a), we extract very important insights: (i) The bulk modulus of a granular assembly can be manipulated by only substituting 5/105% of the base material with fines. (ii) We can control the "direction" of the change (enhanced or lowered bulk modulus) and the magnitude of change through the density and the size of the small particles. (iii) For loose material, there is no enhancement. (iv) For dense material, for a given density, there is an ideal size of fines that leads to the maximum in the bulk modulus.

We associate the different trends observed for loose and dense systems with the ability of the fines (material B) to fill the voids formed by particles A. In the loose state, particles B are smaller than the average void size, so they act as rattlers, and do not contribute to the force network, leading to a decreasing bulk modulus with β. With increasing density, the void size gets smaller and compatible with the size of particles B, and thus contribute to the active contact network (see appendix Appendix A).

The maximum in K observed in Fig. 13(a) is different from that observed in the isotropic fabric F_v shown in Fig. 8. For a uniformly polydisperse systems, the bulk modulus is directly associated with F_v [9], but is not the case for a bidisperse granular mixture with wide size ratio [13].

Fig. 13(b) shows the value of K against v for two extremes: smallest $\beta = \beta_{min}$ and $\beta = 1$ as shown in the legend, both represent monodisperse cases of only A particles. $K(\beta = \beta_{min})$ is the left most data points in Fig. 13(a), increasing with v. For $\beta = 1$, particles B are infinitely small and therefore do not participate in the contact network. Thus, the value $K(\beta = 1)$ is obtained by removing B from the system. This leads to a slightly smaller volume fraction (1/1.05 times the original) and $K(\beta = 1)$ is smaller than $K(\beta = \beta_{min})$ and the two lines being parallel. The

---

[13]Note that pressure decreases monotonically with β, see Fig. 11(b), whereas K has a maximum for higher densities; thus K and P do not have a simple relation (even though both are related to F_v).

two data-sets for the limit cases in Fig. 13(b) show good agreement when fitted by Eq. (25). As already visible in Fig. 13(a), Fig. 13(b) shows that the maximum bulk modulus measured for each volume fraction from Fig. 13(a), does not lie in between of the two extremes $K(\beta = 1)$ is smaller than $K(\beta = \beta_{\min})$.

In order to understand the behavior of K observed in Fig. 13(a), we look at the contributions to the bulk modulus of the three types of contacts present in the system, namely AA, AB and BB. It is straightforward to show that $K = K_{AA} + K_{AB} + K_{BB}$. Since the change in stress on B particles is very small in average, K_{BB} is negligible (data not shown) when the granular assembly is subjected to small perturbation dν, and hence $K \approx K_{AA} + K_{AB}$. Fig. 14(a) shows the bulk modulus for AA and AB interactions, K_{AA} and K_{AB}. K_{AA} remains almost constant with β, except for the smallest ν, where it slightly decreases. K_{AB} remains small for loose system, as B particles mostly are rattlers. For high density, we observe an increase in K_{AB} with β followed by a decrease. This signifies that the trend observed for K in Fig. 13(a) is mainly related to the behavior of AB interactions, while the actual value depends on the contributions of AA main network.

The radius of B, governed by β at a particular volume fraction ν, plays an important role not only in filling the voids of A, but also in contributing to the strong force network, leading to the maxima in bulk modulus K. Now we want to relate the bulk modulus K with the packing properties, in a similar fashion of Eqs. (16) and (23) as adopted for fabric and pressure respectively. We use the relation proposed in [27] to link K to the polydispersity and the mean packing properties of the sample [6, 11]:

$$K = \frac{2\langle r_A \rangle p_0^* g_s \nu^* C^*}{\nu_c \sqrt{\langle r^2 \rangle}} \left[1 - 2\gamma_p \left(-\epsilon_v \right) + \left(-\epsilon_v \right) \left(1 - \gamma_p \left(-\epsilon_v \right) \right) \frac{\partial \ln F_v}{\partial \left(-\epsilon_v \right)} \right], \qquad (26)$$

where $p_0^* = 0.043$, $\gamma_p = 0.2$ are constant fit parameters taken from Refs. [6, 8, 9] and the ν_c is the jamming volume fraction. g_s is the size distribution factor and for our bidisperse distribution is given by (see appendix Appendix B) [27]:

$$g_s = \frac{\langle r \rangle}{\langle r^3 \rangle} \frac{r_A^2 \Omega_A^{-1} f_A + r_B^2 \chi \Omega_B^{-1} f_B}{\Omega_A^{-1} f_A + \chi \Omega_B^{-1} f_B} = \frac{\langle r \rangle \langle r^2 \rangle_g}{\langle r^3 \rangle}. \qquad (27)$$

where the same modification for χ as given in Eq. (18) has been adopted [14]. Fig. 14(b) shows the variation in g_s with β for different volume fractions ν. g_s starts from 1 and decreases with β, with $g_s = 1$ recovered only for small densities at larger β, when the system behaves like an assembly of only A particles and B do not contribute to the contact network (rattlers), see also in Fig. 3. For dense states, g_s decreases continuously and reaches 0.75. The asymptotic value of g_s where also rattlers are considered diverges with $1 - \beta$ with power law -1/3, dotted lines in Fig. 14(b). It is worthwhile to notice that the g_s in Eq. (27) is different from g_3 as used in Eq. (17) for isotropic fabric F_v, meaning that bulk modulus and fabric depend on the polydispersity in a different fashion. In Fig. 13(a), the prediction of Eq. (26) is reported and an excellent agreement is found. It is noteworthy that neglecting the particle polydispersity via g_s over-predicts the bulk modulus as much as 25%. Note that in Eq. (26) a constant p_0^* is used, while this is not the case for extreme polydispersity in our system (see Fig. 12(a)). Future research will focus developing analytical relation for K from Eq. (23), where the dependence of p_0 on volume fraction ν is also considered.

---

[14]For a uniform distribution, g_s is very close to unity and is independent of the width of the distribution. That may be the reason it did not appear in Refs. [6, 11].

7. Qualitative Results

This paragraph is devoted to the qualitative discussion of the findings of this study.

Starting from a base assembly consisting of particles A, a certain volume is substituted with smaller size particles B, while the total volume is kept constant. We restrict ourselves to a small amount of additives (5/105=4.76%), i.e., much less material than would be necessary to fill the pore-space in the base material and focus on the effect of particle size-ratio. We study the two limits of either similar sizes ($r_B \sim r_A$) and of very small sized B ($r_B \ll r_A$), as well as the interesting regime in between the limits.

Substituting A with similar sized particles B is unlikely to change the system properties significantly, since the new particles fully participate in the mixture (besides a few rattlers). Thus, we observe a small effect of the polydispersity due to the new species on the bulk properties. On the contrary, when substituting with very small particles B, the mechanical properties of the mixture are practically the same as fewer (1/1.05) of the base material A alone, since the B particles are so small that they can move in between particles A, freely passing through the pore-throats and thus escaping the pores whenever necessary to reduce their stress. In the intermediate size-regime (roughly $1/2 > r_B/r_A > 1/5$) a little volume of particles B can change the mixture properties considerably, providing systems with higher mechanical bulk modulus as compared to the mere interpolation between the two limit cases.

Assume a pore-size distribution with most pores (formed by A) between a cubic and a hexagonal local structure, such that they can accommodate particles of sizes between $r_8 = (\sqrt{3}-1)r_A \approx 0.732r_A$ and $r_6 = (\sqrt{3/2}-1)r_A \approx 0.225r_A$, respectively (see appendix Appendix A for discussion on the pore sizes corresponding to different packing arrangements). Thus, the typical pore-size is $r_p/r_A \approx (r_8 + r_6)/2r_A \approx 0.48$, while there are no pores outside of this range.

There are two possibilities to scan the range of pores for a given volume of substitution. One can either change (*i*) the size of particle B, r_B (or β) or (*ii*) the size of the pores (by changing the volume of the sample).

(*i*) Assuming fixed volume of the system, for $r_B > r_8$, any particle B sitting in a pore between particles A will mechanically contribute to the packing, and we are in the large size of particle B limit. When decreasing r_B below r_8, more and more pores will lose the mechanical contact with their (caged or trapped) particles B, until, for $r_B \sim r_6$, practically all pores filled with single particles B have lost contact with their cages. However, pores filled with more than one particle B still could contribute to the force network, so that the number of particles B becomes important (which is considerably increasing with decreasing size r_B). When $r_B < r_4 = (\sqrt{2}-1)r_A \approx 0.414r_A$ also multiple B particles lose their efficiency, since they can escape through square pores and for $r_B < r_3 = (2/\sqrt{3} - 1)r_A \approx 0.155r_A$ even through the smallest triangle pores, i.e., we are in the small β limit.

(*ii*) For a fixed size of particles B, increasing the volume fraction (decreasing the volume) will reduce the available pore sizes and thus shift the whole phenomenology towards smaller r_B. All pores become smaller and, for the largest densities used, the smallest pore-throats r_3 are almost closed so that the escape mechanism is hindered, but not blocked since there are still other (e.g. square) shaped throats in the (disordered, non-crystalline) packings. The reduction in pore size is proportional to the typical AA-contact deformation, which in turn is proportional to the pressure (first order) and thus to the density relative to the jamming density.

Combining the two cases, the maximal bulk modulus K of the packings, as function of volume fraction, occurs at $r_B \propto r_p(1 - \delta_{AA}/r_A) \approx r_p(1 - \ln(\nu/\nu_c))$. Furthermore, we attribute the

16

increase of the maximal K with increasing volume fraction ν to the reduced mobility of the small particles, due to shrinking pores and pore throats.

Fig. 15 shows the variation in the bulk modulus K, against r_B/r_A for different volume fractions. For dense assemblies, K attains maxima near the size ratio corresponding to tetrahedron configurations, meaning that the dense state is more likely (possibly due to ongoing crystallization) to create such a configuration and this is the efficient mean arrangement. For the looser systems, the maximum of K moves towards higher size ratios r_B/r_A, corresponding to cubic-like configurations.

8. Conclusion and Outlook

In this study, we used DEM simulations to study the bulk properties of a granular assembly, initially composed of monodisperse particles. A fixed volume fraction of them were substituted with $5/105=4.76\%$ of fines, in order to create a bidisperse mixture. The focus was on designing mixtures with improved bulk properties with minimal costs/alterations by substituting a part of it by a tiny amount of fines in the assembly. The system can be characterized by the number ratio $\beta = N_B^T / \left(N_A^T + N_B^T \right)$ of fines to the total number of particles (or alternatively by the size ratio) and we studied the combined effects of β and volume fraction (consolidation) on the micro- and macroscopic properties of the mixture.

Important highlights regarding microscopic and macroscopic (bulk) information of granular mixtures are: The static pressure due to repulsive particle interactions and the coordination number (excluding rattlers) decrease monotonically with β, with vanishing variations for $\beta \to 1$. The isotropic fabric F_v, a measure of the contact network density, decreases with β for loose systems (similar to the behavior of pressure), since large pores created by big particles provide space for fines to be 'caged'. The behavior for higher densities is different, as F_v first increases with β and then decreases for $\beta \to 1$. In the first stage, the system is more coordinated and fines efficiently pack the voids, while when $\beta \to 1$, most fines become rattlers, and thus F_v decreases. The fabric is well described by the relation $F_v = g_3^\chi \nu^* C^*$, similar to the relation for smooth, continuous polydisperse size distribution introduced in Refs. [6, 8, 9, 27], when $g_3^\chi \neq g_3$ is properly modified with a non-constant compacity accounting for very large size ratios and correspondingly many small rattlers.

Finally, we focus on the effective bulk modulus K, measured by applying small volumetric perturbations to the system. The behavior of K is qualitatively different from both pressure and fabric. For loose systems, a monotonous decrease is observed, while for denser systems, K first increases, reaching a maximum, depending on the density of the sample, and later decreases. The limit $\beta = 1$ can be thought of as the case of infinitely small fines and thus resembles the monodisperse case with volume fraction reduced by $1/1.05$ with respect to the original case.

In this study, the focus was on the bulk properties of a granular assemblies with different size ratios when only a small (fixed) volume of fines is included. We used the simple linear-spring-dashpot contact model with background dissipation excluding all the non-linearities present in the system due to more realistic contact models to be able to focus on and develop the non-linear scaling laws for macroscopic observations from microscopic informations. Next step is studying the influence of different volumes of fines on the material behavior, that is to explore different regimes of coarse-fine mixture ratios. Using more realistic, non-linear contact models with friction and cohesion is a necessary extension to model real materials. Another interesting extension of this study would be to consider a "hierarchical granular medium" in which the

particle size distribution is engineered to obtain required mechanical properties, e.g. the bulk or shear modulus. Finally, the focus can be moved towards other loading paths (e.g. uniaxial compression or shear tests) to study the effect fine content and modes of deformation on the evolution of the full elastic tensor.

Acknowledgement

Appendix A. Radius ratio in different lattice configurations

In this appendix, we focus on the possible arrangements of particles A and B in the granular assembly in order to characterize some special sizes of voids in the sample. At a given density, particles A create voids whose size depends on the geometry. Among the many possible arrangements of A, few possibilities are triangular, tetrahedron, square and cubic lattices as shown in Fig. A.1. Particles B can efficiently fill these voids at special ratios between the void size and the radius of A.

Fig. A.1.(a) shows a configuration where three A particles are arranged in a plane forming a triangular lattice and one particle B of radius r_3 is located in the void, centered at O, and touches A particles. Thus,

$$AP = AO\cos(\angle PAO) = AO\cos(30°),$$

that means:

$$r_A = (r_A + r_3)\frac{\sqrt{3}}{2}.$$

From here we can obtain the size ratio such that B efficiently fills the pore throat formed by three A:

$$\frac{r_3}{r_A} = \frac{2}{\sqrt{3}} - 1 \approx 0.155. \tag{A.1}$$

Fig. A.1.(b) shows a sample configuration where A particles are arranged in a tetrahedron lattice i.e., a local hexagonal structure, with three of them on a plane while the fourth is out of the plane. Assuming the tetrahedron is centered at the origin O, that is also the center of particle B of radius r_6, while AB is one side of the tetrahedron and connects the centers of two A particles, ($AB = 2r_A$). The four vertices of the tetrahedron are $r_A\left(\pm 1, 0, -1/\sqrt{2}\right)$ and $r_A\left(0, \pm 1, 1/\sqrt{2}\right)$. The tetrahedral angle $\angle AOB$ is $\arccos(-1/3) \approx 109.47°$. Using the law of cosines we get

$$AB^2 = AO^2 + OB^2 - 2.AO.OB\cos(\angle AOB),$$

that in terms of radii becomes:

$$(r_A + r_A)^2 = (r_A + r_6)^2 + (r_A + r_6)^2 - 2(r_A + r_6)(r_A + r_6)\cos(\arccos(-1/3))$$

$$= (r_A + r_6)^2\left(1 + 1 - 2\left(\frac{-1}{3}\right)\right) = \frac{8}{3}(r_A + r_6)^2.$$

18

The tetrahedron void ratio is thus:

$$\frac{r_6}{r_A} = \sqrt{\frac{3}{2}} - 1 \approx 0.225. \tag{A.2}$$

Next in Fig. A.1.(c), we show a configuration where A particles are arranged in a planar square lattice and particle B of radius r_4 sits in the void of A. Using Pythagoras' theorem, the relation between the sides of the lattice is:

$$AB^2 = AO^2 + OB^2 = 2AO^2,$$

and introducing the radii

$$(r_A + r_A)^2 = 2\,(r_A + r_4)^2\,,$$

and the size ratio for efficient packing is

$$\frac{r_4}{r_A} = \sqrt{2} - 1 \approx 0.414. \tag{A.3}$$

Finally, Fig. A.1.(d) shows a configuration where A particles are arranged in a body centered lattice with particle B of radius r_8 in the center of the cube touching A. Using again Pythagoras theorem, we can write

$$AG^2 = AD^2 + DG^2 = AD^2 + CD^2 + CG^2 = 3AD^2,$$

and

$$(2r_A + 2r_8)^2 = 3\,(r_A + r_A)^2\,,$$

that leads to the cubic void size ratio:

$$\frac{r_8}{r_A} = \sqrt{3} - 1 \approx 0.732. \tag{A.4}$$

By comparing the four cases considered here, the triangular lattice produces the smallest size ratio $r_3/r_A \approx 0.155$ while the cubic lattice $r_8/r_A \approx 0.732$ creates the largest one.

For the case of overlapping spheres, the size ratio must be corrected by including the average overlap between AA ($\langle \delta_{AA} \rangle$) and AB ($\langle \delta_{AB} \rangle$) interactions.

Appendix B. Measurement of g_3 and g_s for fabric and bulk modulus

We are interested in relating the isotropic fabric with the mean packing properties (coordination number and volume fraction) via $F_v = g_3 \nu C$. The continuous limit of Eq. (15) is given by [27]:

$$F_v = \frac{N_4}{V} \int_0^\infty V(r)C(r)f(r)dr = g_3 \nu^* C^*, \tag{B.1}$$

where $C(r)$ is the coordination number of a particle with radius r, volume $V(r) = 4\pi r^3/3$ and $f(r)$ is the particle size (radii) distribution defined in section 4.4. The corrected volume fraction in the continuous form is given as:

$$\nu^* = \frac{N_4 \int_0^\infty V(r)f(r)dr}{V}. \tag{B.2}$$

19

Let's assume that a reference p-particle with radius r in the system has a contact with a neighboring particle of average radius $\langle r \rangle$. The space angle covered by the neighboring particle on the reference particle in a three-dimensional packing of sphere is given as [6, 27]:

$$\Omega(r) = 2\pi \left(1 - \sqrt{1 - \left(\frac{\langle r \rangle}{r + \langle r \rangle} \right)^2} \right), \tag{B.3}$$

and the linear compacity (or the fraction of the shielded surface) associated with a single interaction is:

$$c_s(r) = \frac{1}{4\pi r^2} \Omega(r) r^2. \tag{B.4}$$

The total compacity of the reference p-particle interacting with its $C(r)$ non-rattler neighboring particle of average radius $\langle r \rangle$ thus becomes:

$$c_s(r) = \frac{1}{4\pi r^2} \sum_{p=1}^{C(r)} \Omega(r) r^2 = \frac{\Omega(r) C(r)}{4\pi}. \tag{B.5}$$

$c_s(r)$ decreases with r, starting from 1 when $r/\langle r \rangle \to 0$ and reaches a constant value for $r/\langle r \rangle \geq 1$. Refs. [6, 27] have shown that $c_s(r)$ decreases with increasing particle radii and saturates to a constant value $\in [0, 1]$ for large sized particles. It is also dependent on the volume fraction of the system. Large differences in particle number and size ratio affects the linear compacity $c_s(r)$. $c_s(r)$ has two bounds:

i) **Upper bound:** the maximum compacity is reached when a small particle is surrounded by two big particles. Therefore, for the lower bound, $r/\langle r \rangle \to 0$ leading to $\Omega(r) = 2\pi$ and hence $\max[c_s(r)] = 1$.

ii) **Lower bound:** Near the jamming transition (loose states), mainly the big particles remain in the system while the smaller particles act as rattlers. To be mechanically stable, big particles need *six* contacts. Using $r/\langle r \rangle \to 1$, we have $\Omega(r) = 2\pi \left(1 - \sqrt{3}/2 \right)$ and hence $\min[c_s(r)] = \Lambda = \frac{\Omega(r) C(r)}{4\pi} = \frac{2\pi \left(1 - \sqrt{3}/2 \right) 6}{4\pi} = 3 \left(1 - \sqrt{3}/2 \right) \approx 0.4$, generally reached by big particles at low volume fraction, i.e., near the jamming transition. Using the definition for the average coordination number C^* in the continuous limit:

$$C^* = \int_0^\infty C(r) f(r) dr = 4\pi \int_0^\infty \frac{c_s(r) f(r)}{\Omega(r)} dr, \tag{B.6}$$

and using Eq. (B.5), we get

$$C^* = 4\pi \int_0^\infty \frac{c_s(r) f(r)}{\Omega(r)} dr. \tag{B.7}$$

Combining Eqs. (B.2), (B.5) and (B.7) in Eq. (B.1), we have:

$$g_3 = \frac{\int_0^\infty r^3 c_s(r) \Omega(r)^{-1} f(r) dr}{\int_0^\infty c_s(r) \Omega(r)^{-1} f(r) dr \int_0^\infty r^3 f(r) dr}, \tag{B.8}$$

In a similar fashion, we use a correction term g_s as proposed in Ref. [27] to link the bulk modulus K of a granular mixture to the polydispersity as:

$$g_s = \frac{\int_0^\infty r f(r) dr \int_0^\infty r^2 c_s(r) \Omega(r)^{-1} f(r) dr}{\int_0^\infty c_s(r) \Omega(r)^{-1} f(r) dr \int_0^\infty r^3 f(r) dr}. \tag{B.9}$$

Appendix C. Analytical expression for pressure

In order to better understand the final analytical expressions, the stress is rewritten and re-
phrased, starting from the traditional definitions. Revisiting Eq. (21), we have:

$$
\begin{aligned}
p &= \frac{2\langle r\rangle}{3k}\mathrm{tr}(\boldsymbol{\sigma}) \approx \frac{2\langle r\rangle}{3k}\frac{1}{V}\mathrm{tr}\left(\sum_{c=1}^{M_4}\mathbf{l}^c\otimes\mathbf{f}^c\right) = \frac{2\langle r\rangle}{3V}\sum_{c=1}^{M_4}\mathrm{tr}\left(l_c\mathbf{n}^c\otimes\delta_c\mathbf{n}^c\right) \\
&= \frac{2\langle r\rangle}{3V}\sum_{c=1}^{M_4}l_c\delta_c\underbrace{\mathrm{tr}\left(n\otimes\mathbf{n}^c\right)}_{=1} = \frac{2\langle r\rangle}{3V}\sum_{c=1}^{M_4}l_c\delta_c \\
&= \frac{2\langle r\rangle}{3V}\sum_{p=1}^{N_4}\left(r_p\sum_{c=1}^{C_p}\delta_c - \frac{1}{2}\sum_{c=1}^{C_p}\delta_c^2\right),
\end{aligned}
\tag{C.1}
$$

where subscript p and c stand for particles and contacts respectively. Average overlap per contact is:

$$
\langle\delta_c\rangle = \frac{\sum_{p=1}^{N_4}\sum_{c=1}^{C_p}\delta_c}{M_4} = \frac{\sum_{p=1}^{N_4}\sum_{c=1}^{C_p}\delta_c}{N_4 C^*}.
\tag{C.2}
$$

Similarly, for the average squared overlap, one can write:

$$
\langle\delta_c^2\rangle = \frac{\sum_{p=1}^{N_4}\sum_{c=1}^{C_p}\delta_c^2}{M_4} = \frac{\sum_{p=1}^{N_4}\sum_{c=1}^{C_p}\delta_c^2}{N_4 C^*}.
\tag{C.3}
$$

Introducing the average overlap for particle p as:

$$
\phi_p =: \frac{\delta_p}{\langle\delta_p\rangle} = \frac{\sum_{c=1}^{C_p}\delta_c}{\left(\sum_{p=1}^{N_4}\sum_{c=1}^{C_p}\delta_c\right)/\sum_{p=1}^{N_4}} = \frac{\sum_{c=1}^{C_p}\delta_c}{(\langle\delta_c\rangle M_4)/\sum_{p=1}^{N_4}} = \frac{\sum_{c=1}^{C_p}\delta_c}{C^*\langle\delta_c\rangle},
\tag{C.4}
$$

where $\langle\delta_c\rangle$ is the average overlap per contact. Eq. (C.1) then can be written as:

$$
\begin{aligned}
p &= \frac{2\langle r\rangle}{3V}\left(\sum_{p=1}^{N_4}r_p\sum_{c=1}^{C_p}\delta_c - \frac{1}{2}\sum_{p=1}^{N_4}\sum_{c=1}^{C_p}\delta_c^2\right) \\
&= \frac{2\langle r\rangle}{3V}\left(\sum_{p=1}^{N_4}r_p C^*\langle\delta_c\rangle\phi_p - \frac{1}{2}\langle\delta_c^2\rangle N_4 C^*\right) \\
&= \frac{2\langle r\rangle}{3V}\left(N_4 C^*\langle\delta_c\rangle\langle r_p\phi_p\rangle - \frac{1}{2}\langle\delta_c^2\rangle N_4 C^*\right) \\
&= \frac{2\langle r\rangle N_4 C^*\langle\delta_c\rangle}{3V}\left(\langle r_p\phi_p\rangle - \frac{\langle\delta_c^2\rangle}{2\langle\delta_c\rangle}\right)\left[\frac{v^*}{(4\pi/3)N_4\langle r^3\rangle/V}\right] \\
&= \frac{C^* v^*}{4\pi}\frac{\langle r\rangle\langle\delta_c\rangle}{\langle r^3\rangle}\left(2\langle r_p\phi_p\rangle - \frac{\langle\delta_c^2\rangle}{\langle\delta_c\rangle}\right)
\end{aligned}
\tag{C.5}
$$

Introducing the normalized particle radius $\xi_p = r_p/\langle r\rangle$ and overlap $\Delta_c = \delta_c/\langle r\rangle$ leads to:

$$
\begin{aligned}
p &= \frac{C^* v^*}{4\pi}\frac{\langle\Delta_c\rangle}{\langle\xi_p^3\rangle}\left(2\langle\xi_p\phi_p\rangle - \frac{\langle\Delta_c^2\rangle}{\langle\Delta_c\rangle}\right) \\
&= \frac{C^* v^*}{4\pi}\langle\Delta_c\rangle\left(2g_p - b_p\langle\Delta_c\rangle\right)
\end{aligned}
\tag{C.6}
$$

where

$$g_p = \frac{\langle \xi_p \phi_p \rangle}{\langle \xi_p^3 \rangle}, b_p = \frac{1}{\langle \xi_p^3 \rangle} \frac{\langle \Delta_c^2 \rangle}{\langle \Delta_c \rangle^2} \tag{C.7}$$

The normalized average overlap $\langle \Delta_c \rangle$ is logarithmically related to the volume fraction of the present state via as also presented in Refs. [6, 8]

$$\langle \Delta_c \rangle = D(-\varepsilon_v) = D\ln\left(\frac{v}{v_c}\right). \tag{C.8}$$

Fig. C.1.(a) shows the measured average overlap per contact $\langle \Delta \rangle_c$ against $\ln(v/v_c)$ and the slope of the linear line is $D = 0.425$, in consistent with the measured value in Ref. [8]. Therefore, Eq. (C.6) can be written in the same form as given in Ref. [6]:

$$p = p_0 \frac{v^* C^*}{v_c} (-\varepsilon_v) \left[1 - \gamma_p(-\varepsilon_v)\right] \tag{C.9}$$

where $p_0 = v_c g_p D/2\pi$ and $\gamma_p = bD/2g_p$. The unknowns are g_p and b_p. Assuming that total force on a particle is proportional to square of contacts it has with neighbors [27], $\delta_p \propto C_p^2$, hence $\phi_p = C_p^2/\langle C_p^2 \rangle$, where $C(r) = 4\pi \frac{c_s(r)}{\Omega(r)}$ (see appendix Appendix B). Therefore, for a continuous distribution, g_p is given as:

$$g_p = \frac{\langle r \rangle^2}{\langle r^3 \rangle} \frac{\int_0^\infty r c_s(r)^2 \Omega(r)^{-2} f(r) dr}{\int_0^\infty c_s(r)^2 \Omega(r)^{-2} f(r) dr}, \tag{C.10}$$

which for a bidisperse size distribution is:

$$g_p = \frac{\langle r \rangle^2}{\langle r^3 \rangle} \frac{r_A \Omega_A^{-2} f_A + r_B^3 \chi^2 \Omega_B^{-2} f_B}{\Omega_A^{-2} f_A + \chi^2 \Omega_B^{-2} f_B}, \tag{C.11}$$

where r_A and r_B are the radius of A and B with number fraction f_A and f_B respectively. Note that the second term in Eq. (C.6) is very small (maximum 10% for dense volume fractions) and is a subject of future research. g_p measured from the simulations is plotted in Fig. C.1.(b) against Eq. (C.11) and the results are in close agreement.

[1] M. Belkhatir, A. Arab, N. Della, and T. Schanz. Experimental Study of Undrained Shear Strength of Silty Sand: Effect of Fines and Gradation. *Geotechnical and Geological Engineering*, 30:1103–1118, 2012.

[2] C. S. Chang and Z.-Y. Yin. Micromechanical modeling for behavior of silty sand with influence of fine content. *International Journal of Solids and Structures*, 48:2655–2667, 2011.

[3] P. A. Cundall and O. D. L. Strack. A discrete numerical model for granular assemblies. *Géotechnique*, 29:47–65, 1979.

[4] J. Fannin. Karl Terzaghi: from theory to practice in geotechnical filter design. *Journal of geotechnical and geoenvironmental engineering*, 134:267–276, 2008.

[5] R. Fuchs, T. Weinhart, J. Meyer, H. Zhuang, T. Staedler, X. Jiang, and S. Luding. Rolling, sliding and torsion of micron-sized silica particles: experimental, numerical and theoretical analysis. *Granular Matter*, 16:281–297, 2014.

[6] F. Göncü, O. Durán, and S. Luding. Constitutive relations for the isotropic deformation of frictionless packings of polydisperse spheres. *C. R. Mécanique*, 338:570–586, 2010.

[7] A. B. Hopkins, F. H. Stillinger, and S. Torquato. Disordered strictly jammed binary sphere packings attain an anomalously large range of densities. *Phys. Rev. E*, 88:022205, 2013.

[8] O. I. Imole, N. Kumar, V. Magnanimo, and S. Luding. Hydrostatic and Shear Behavior of Frictionless Granular Assemblies Under Different Deformation Conditions. *KONA Powder and Particle Journal*, 30:84–108, 2013.

[9] N. Kumar, O. I. Imole, V. Magnanimo, and S. Luding. Effects of polydispersity on the micro-macro behavior of granular assemblies under different deformation paths. *Particuology*, 12:64–79, 2014.

[10] N. Kumar and S. Luding. Memory of jamming-multiscale flow in soft and granular matter. *arXiv preprint arXiv:1407.6167*, 17.

[11] N. Kumar, S. Luding, and V. Magnanimo. Macroscopic model with anisotropy based on micromacro information. *Acta Mechanica*, 225:2319–2343, 2014.

[12] P. V. Lade, C. D. Liggio, and J. A. Yamamuro. Effects of non-plastic fines on minimum and maximum void ratios of sand. *Geotechnical Testing Journal*, 21:336–347, 1998.

[13] S. Luding. Anisotropy in cohesive, frictional granular media. *Journal of Physics Condensed Matter*, 17:S2623–S2640, 2005.

[14] S. Luding. Cohesive, frictional powders: contact models for tension. *Granular Matter*, 10:235–246, 2008.

[15] M. Madadi, O. Tsoungui, M. Latzel, and S. Luding. On the fabric tensor of polydisperse granular materials in 2D. *International Journal of Solids and Structures*, 41:2580, 2004.

[16] C. L. Martin and D. Bouvard. Isostatic compaction of bimodal powder mixtures and composites. *International Journal of Mechanical Sciences*, 46:907–927, 2004.

[17] N. H. Minh, Y. P. Cheng, and C. Thornton. Strong force networks in granular mixtures. *Granular Matter*, 16:69–78, 2014.

[18] F. J. Muzzio, T. Shinbrot, and B. J. Glasser. Powder technology in the pharmaceutical industry: the need to catch up fast. *Powder Technology*, 124:1–7, 2002.

[19] Q. Ni, T. S. Tan, G. R. Dasari, and D. W. Hight. Contribution of fines to the compressive strength of mixed soils. *Géotechnique*, 54:561–569, 2004.

[20] V. Ogarko and S. Luding. Equation of state and jamming density for equivalent bi- and polydisperse, smooth, hard sphere systems. *Journal of Chemical Physics*, 136, 2012.

[21] V. Ogarko and S. Luding. Prediction of polydisperse hard-sphere mixture behavior using tridisperse systems. *Soft Matter*, 9:9530–9534, 2013.

[22] C. S. O'Hern, L. E. Silbert, A. J. Liu, and S. R. Nagel. Jamming at zero temperature and zero applied stress: The epitome of disorder. *Phys. Rev. E*, 68:011306, 2003.

[23] K. C. E. Östergren, A. C. Trägaardh, G. G. Enstad, and J. Mosby. Deformation of a chromatographic bed during steady-state liquid flow. *AIChE journal*, 44:2–12, 1998.

[24] F. Radjai, D. E. Wolf, M. Jean, and J. Moreau. Bimodal Character of Stress Transmission in Granular Packings. *Phys. Rev. Lett.*, 80:61, 1998.

[25] M. M. Rahman, S. R. Lo, and M. A. Baki. Equivalent granular state parameter and undrained behaviour of sand-fines mixtures. *Acta Geotechnica*, 6:183–194, 2011.

[26] R. Salgado, P. Bandini, and A. Karim. Shear strength and stiffness of silty sand. *Journal of Geotechnical and Geoenvironmental Engineering*, 126:451–462, 2000.

[27] M. R. Shaebani, M. Madadi, S. Luding, and D. E. Wolf. Influence of polydispersity on micromechanics of granular materials. *Phys. Rev. E*, 85:011301, 2012.

[28] P. Shao, K. Darcovich, T. McCracken, G. Ordorica-Garcia, M. Reith, and S. O'Leary. Algae-dewatering using rotary drum vacuum filters: Process modeling, simulation and techno-economics. *Chemical Engineering Journal*, 268:67–75, 2015.

[29] T. Shire, C. O'Sullivan, K. J. Hanley, and R. J. Fannin. Fabric and effective stress distribution in internally unstable soils. *Journal of Geotechnical and Geoenvironmental Engineering*, 140:04014072, 2014.

[30] A. Singh, V. Magnanimo, K. Saitoh, and S. Luding. Effect of cohesion on shear banding in quasistatic granular materials. *Phys. Rev. E*, 90:022202, 2014.

[31] S. Thevanayagam, T. Shenthan, S. Mohan, and J. Liang. Undrained fragility of clean sands, silty sands, and sandy silts. *Journal of geotechnical and geoenvironmental engineering*, 128:849–859, 2002.

[32] T. Ueda, T. Matsushima, and Y. Yamada. Effect of particle size ratio and volume fraction on shear strength of binary granular mixture. *Granular Matter*, 13:731–742, 2011.

[33] L. E. Vallejo. Interpretation of the limits in shear strength in binary granular mixtures. *Canadian Geotechnical Journal*, 38:1097–1104, 2001.

[34] W. M. Yan and J. Dong. Effect of particle grading on the response of an idealized granular assemblage. *International Journal of Geomechanics*, 11:276–285, 2011.

[35] Z.-Y. Yin, J. Zhao, and P.-Y. Hicher. A micromechanics-based model for sand-silt mixtures. *International Journal of Solids and Structures*, 51:1350–1363, 2014.
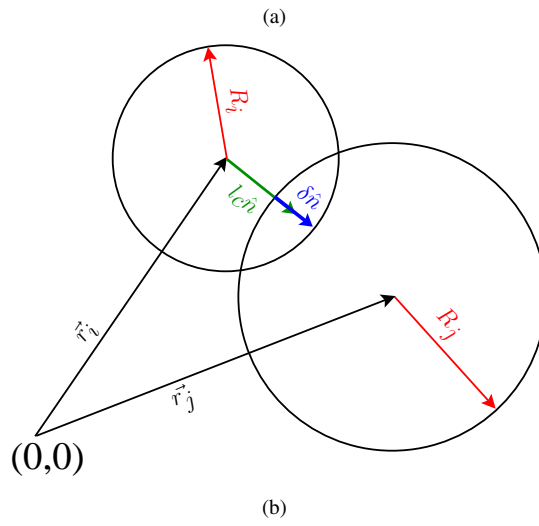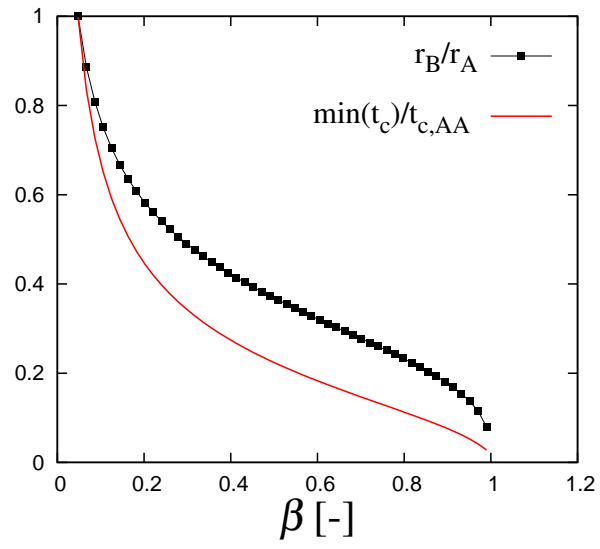
Figure 1: (a) Variation of the radius ratio r_B/r_A and smallest collision duration t_c with $\beta = N_B^T/\left(N_A^T + N_B^T\right)$. (b) Sketch of two particles in contact and the direction of the force and branch vectors.

(a)

(b)

(c)

(d)

(e)

(f)
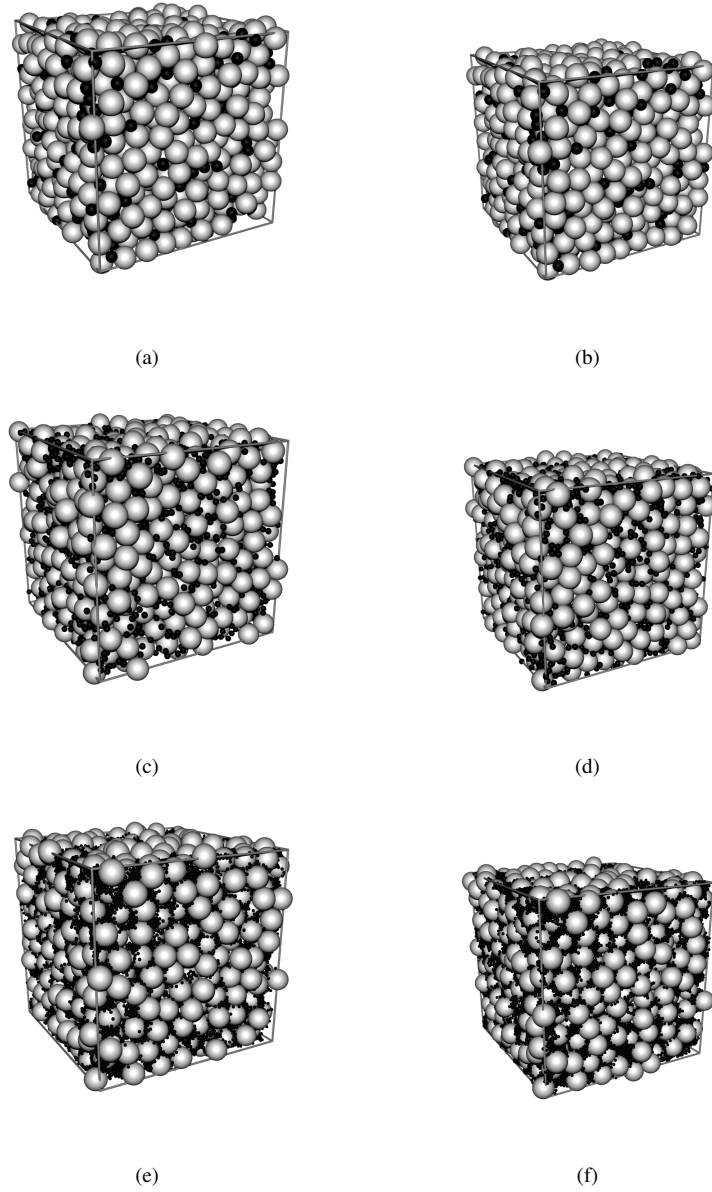
Figure 2: Snapshots of the composite material. White and black particles are particles of A (large) and B (small), respectively. Different rows represent different $\beta = N_B^T / \left(N_A^T + N_B^T \right) = 0.075$, 0.56, and 0.96, with size ratio $r_B/r_A = 0.5$, 0.27 and 0.14. Left and right columns correspond to total volume fractions $\nu = 0.69$ (loose) and 0.82 (dense), respectively.

(a)

(b)

(c)

(d)

(e)

(f)
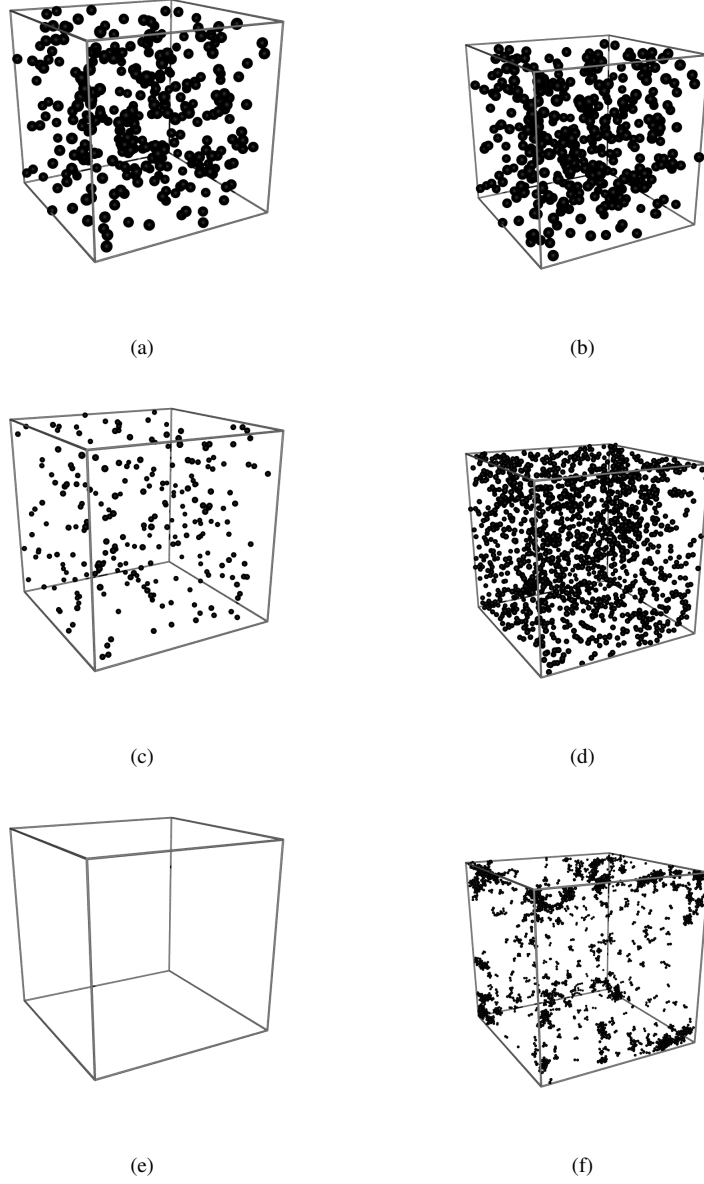
Figure 3: Snapshots of the fines (same as Fig. 2) without rattlers, i.e., for clarity only particles B are shown. Different rows represent different $\beta = N_B^T / \left(N_A^T + N_B^T \right) = 0.075$, 0.56, and 0.96, with size ratio $r_B/r_A = 0.5$, 0.27 and 0.14. Left and right columns correspond to total volume fractions $\nu = 0.69$ and 0.82, respectively.
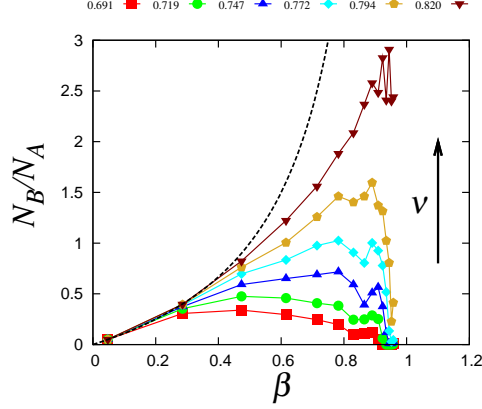
Figure 4: Ratio of B particles with respect A: N_B/N_A, when the assembly contains no rattlers; the dashed line considers also rattlers (see Eq. (3)), i.e., N_B^T/N_A^T. All are plotted against the number fraction $\beta = N_B^T/\left(N_A^T + N_B^T\right)$. Different colors represent the volume fraction ν as shown in the legend and the arrow indicates increasing ν.
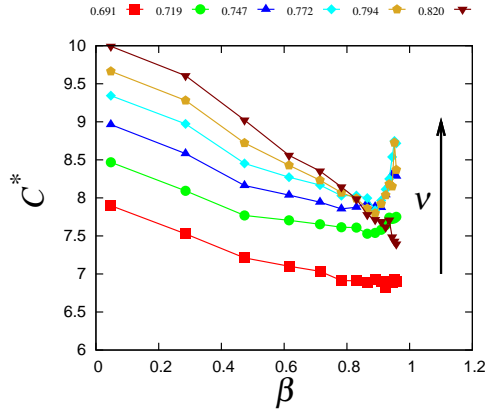
Figure 5: Coordination number excluding rattlers plotted against the number fraction $\beta = N_B^T/\left(N_A^T + N_B^T\right)$. Different colors represent the volume fraction ν as shown in the legend and the arrow indicates increasing ν.

(a)   (b)   (c)
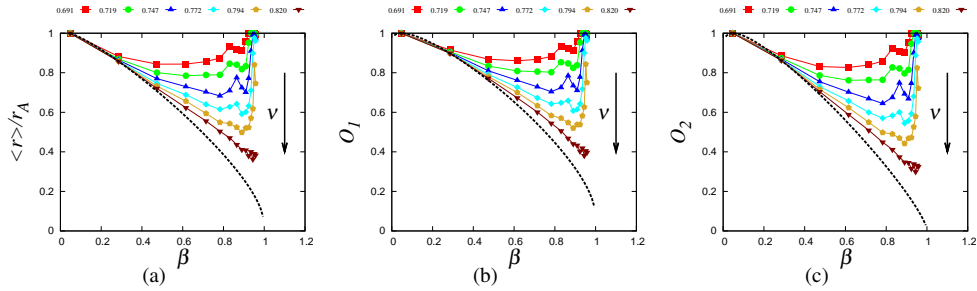
Figure 6: (a) Average radius $\langle r \rangle$ scaled by r_A; dimensionless moments (b) O_1 and (c) O_2, measured using Eq. (5), excluding rattlers, plotted against the number fraction $\beta = N_B^T/\left(N_A^T + N_B^T\right)$. Different colors represent the volume fraction ν as shown in the legend. The dashed lines that consider also rattlers are Eqs. (7) and (8). The arrows indicate increasing ν.

28
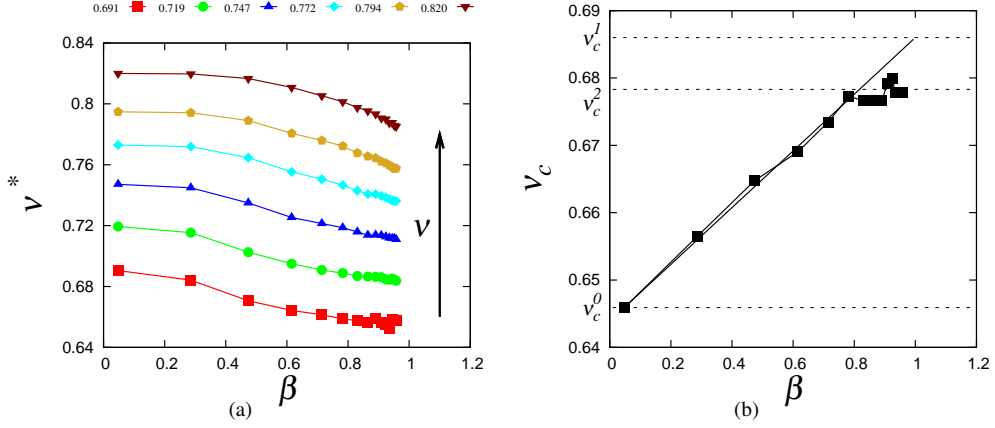
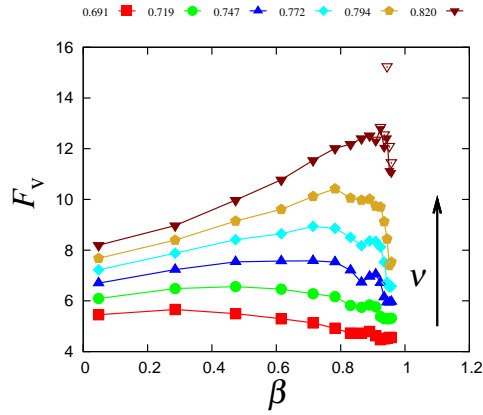Figure 7: (a) Volume fraction ν^* of the system excluding rattlers plotted against the number fraction $\beta = N_B^T / (N_A^T + N_B^T)$. Different colors represent the volume fraction ν as shown in the legend and the arrow indicates increasing ν. (b) Evolution of jamming point ν_c with β. The solid line is a linear fit to the simulation data using Eq. (11). The dashed horizontal lines are: ν_c^0 for the smallest β, ν_c^1 fit parameter obtained for $\beta \to 1$ and ν_c^2 is the estimated value for $\beta \to 1$ using Eq. (12) when the system contains only particles A.

Figure 8: Isotropic fabric F_v plotted against the number fraction $\beta = N_B^T / (N_A^T + N_B^T)$. Different colors represent the volume fraction ν as shown in the legend and arrow indicates increasing ν. Open symbols are corresponding F_v^T that includes the rattlers as well.
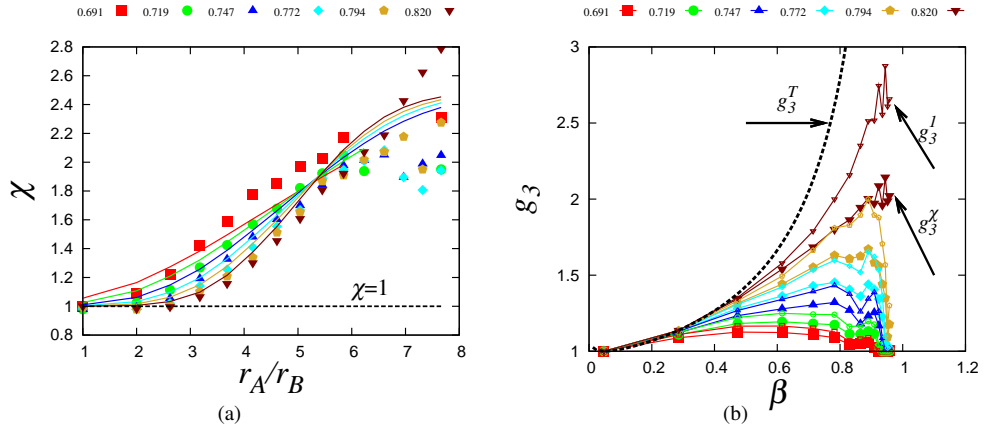
Figure 9: (a) Ratio of linear compacities of particles B to A, χ, versus the radius ratio r_A/r_B measured from the DEM simulations (symbols) and the corresponding line is the analytical fit to the data using Eq. (18). The dashed line is constant linear compacity, i.e., $\chi = 1$. (b) g_3^χ for fabric calculated using Eqs. (17) with χ estimated using (18) (solid symbols) and g_3^1 measured from constant linear compacity assumption $\chi = 1$ (small open symbols), plotted against the number fraction $\beta = N_B^T / \left(N_A^T + N_B^T \right)$ excluding the rattlers. Different colors represent the volume fraction ν as shown in the legend. The dashed line is g_3^T and considers also rattlers.
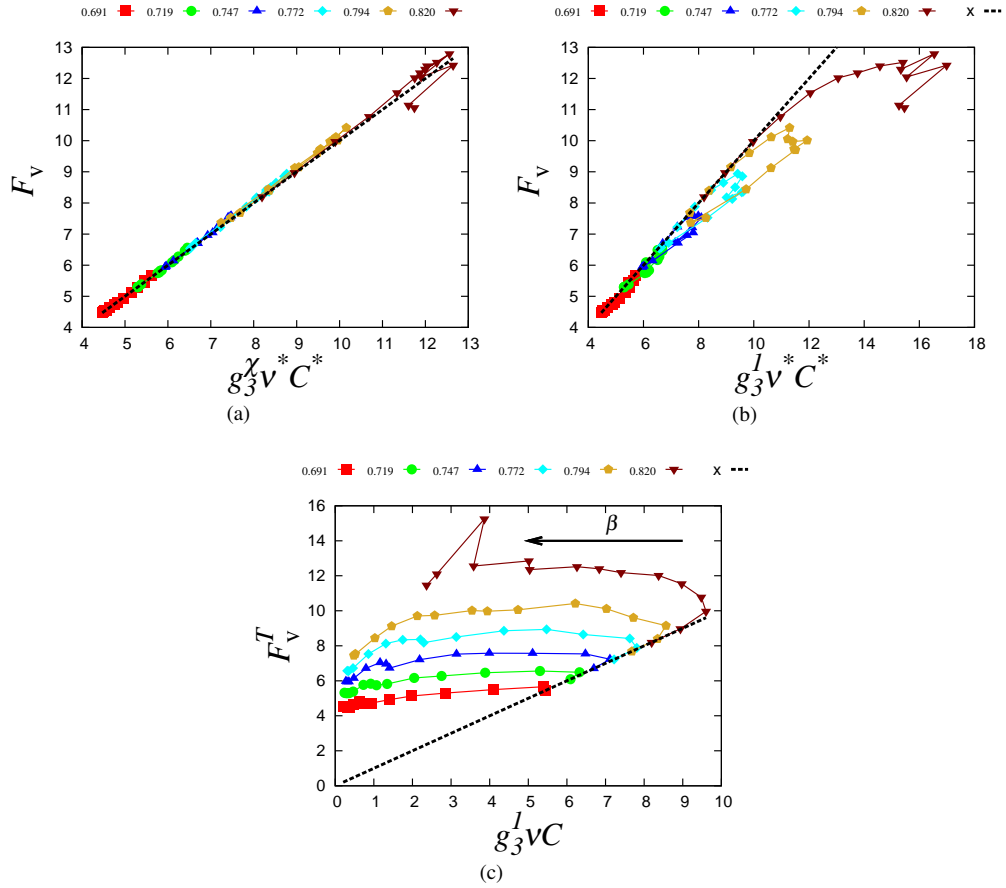
Figure 10: Isotropic fabric F_v plotted against Eq. (16) with g_3^χ calculated using Eq. (17) with (a) non-constant linear compacity, with χ computed based on volume fraction and radius ratio using Eq. (18) and (b) constant linear compacity, with $\chi = 1$. The dashed black line has slope 1. Different colors represent the volume fraction ν as shown in the legend. (c) The total isotropic fabric including the rattlers F_v^T compared to the relation presented in Ref. [6], and the arrow indicates increasing β.

31
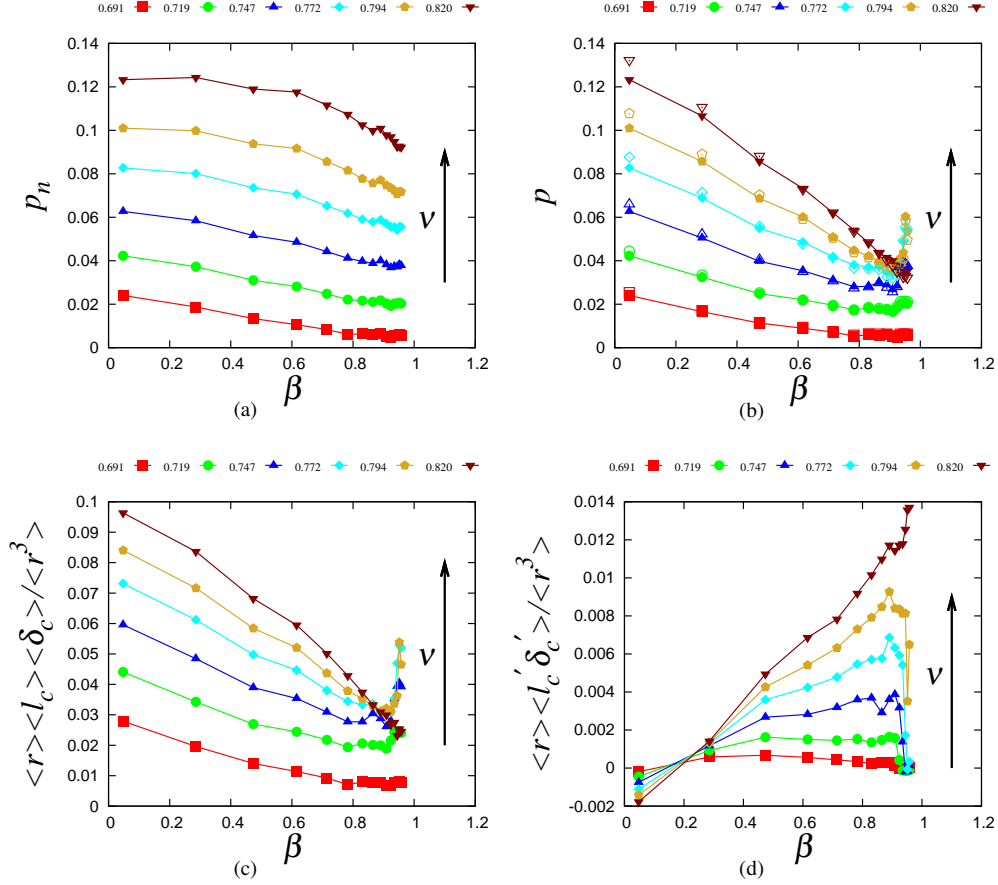
Figure 11: (a) Non-dimensional pressure (scaled by constant $2\langle r_A \rangle / k$) p_n, (b) non-dimensional pressure p scaled by $2\langle r \rangle / k$ (solid symbols) and prediction using Eq. (23) (open symbols) (c) product of mean radius $\langle r \rangle$, branch vector $\langle l_c \rangle$ and particle overlap $\langle \delta_c \rangle$ scaled with the third moment $\langle r^3 \rangle$ and (d) product of mean radius $\langle r \rangle$ and the corresponding fluctuation term $\langle l'_c \delta'_c \rangle$ scaled with the third moment $\langle r^3 \rangle$, calculated using Eq. (22), plotted against the number fraction $\beta = N_B^T / \left(N_A^T + N_B^T \right)$. Different colors represent the volume fraction ν as shown in the legend and arrows indicate increasing ν.
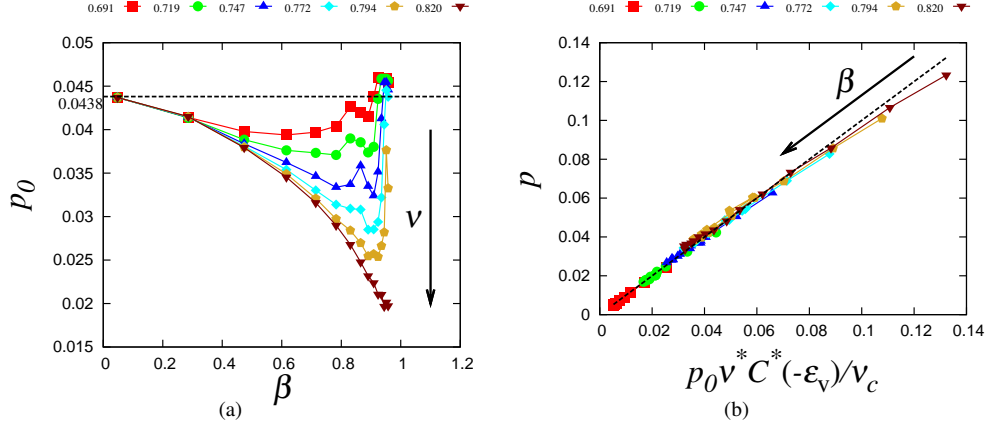
Figure 12: (a) Measured p_0 plotted against the number fraction $\beta = N_B^T / \left(N_A^T + N_B^T \right)$. The dashed line represents the constant value of p_0 for the monodisperse case. The arrow indicates increasing ν (b) Non-dimensional pressure p plotted against Eq. (23) without the second term. The dashed linear line has slope 1 and the arrow indicates increasing β. Different colors represent the volume fraction ν as shown in the legend.
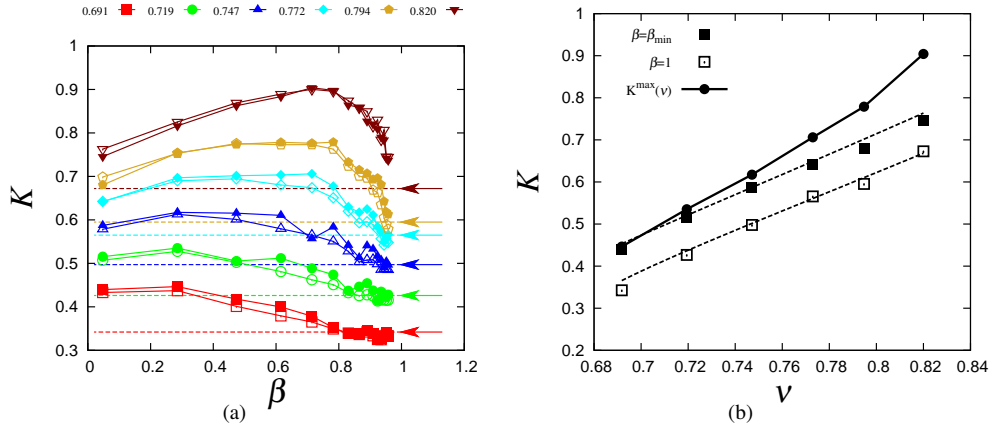

Figure 13: (a) Bulk modulus (scaled by constant $2\langle r_A \rangle / k$) K measured using Eq. (25) (solid symbols) and predicted using Eq. (26) for the whole system plotted against the number fraction $\beta = N_B^T / \left(N_A^T + N_B^T \right)$. Different colors represent the volume fraction ν as shown in the legend. The corresponding arrows show K for $\beta = 1$, i.e., the limit for infinitely small B particles, where the measurements are done after removing all the small particles and the static assembly consisted of only A. (b) K for the two extreme cases: $\beta = \beta_{\min}$ (solid symbols) and $\beta = 1$ (empty symbols), both are the monodisperse cases with the latter having 5% fewer particles than the former. Lines passing through the data is Eq. (25). The dots represents the maximum K obtained from (a) for a given density.
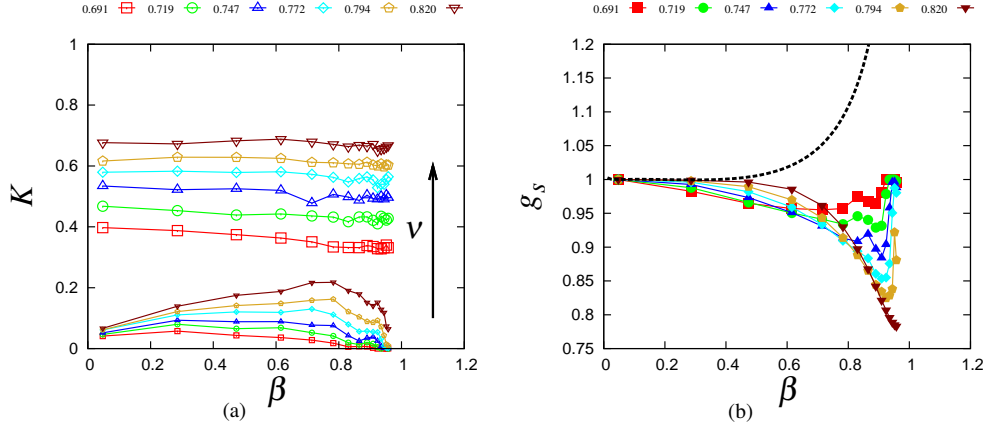
33

Figure 14: (a) Partial bulk modulus (scaled by constant $2\langle r_A \rangle/k$) for the AA (big symbols) and AB (small symbols) interactions, plotted against the number fraction $\beta = N_B^T / \left(N_A^T + N_B^T \right)$, from the same data as in Fig. 13(a). (b) g_s calculated using Eq. (27), where the dashed line is Eq. (27) with constant linear compacity assumption, i.e., $\chi = 1$ for the total mixture including the rattlers, see Eq. (3).
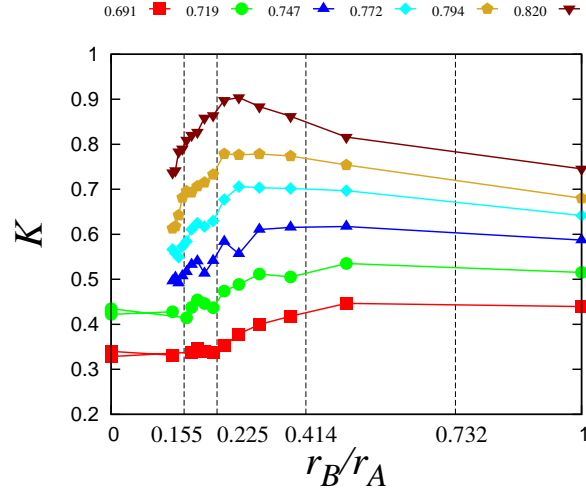

Figure 15: Bulk modulus (scaled by constant $2\langle r_A \rangle/k$) measured using Eq. (25) plotted against size ratio r_B/r_A. The dashed vertical lines represent the radio ratio when particle B fills the void by A formed in triangular, tetrahedron, square and cubic lattices respectively, as shown in Fig. A.1. Different colors represent the volume fraction ν as shown in the legend. For the two lowest loose states, all B particles are rattlers and hence $r_B = $ in the system.
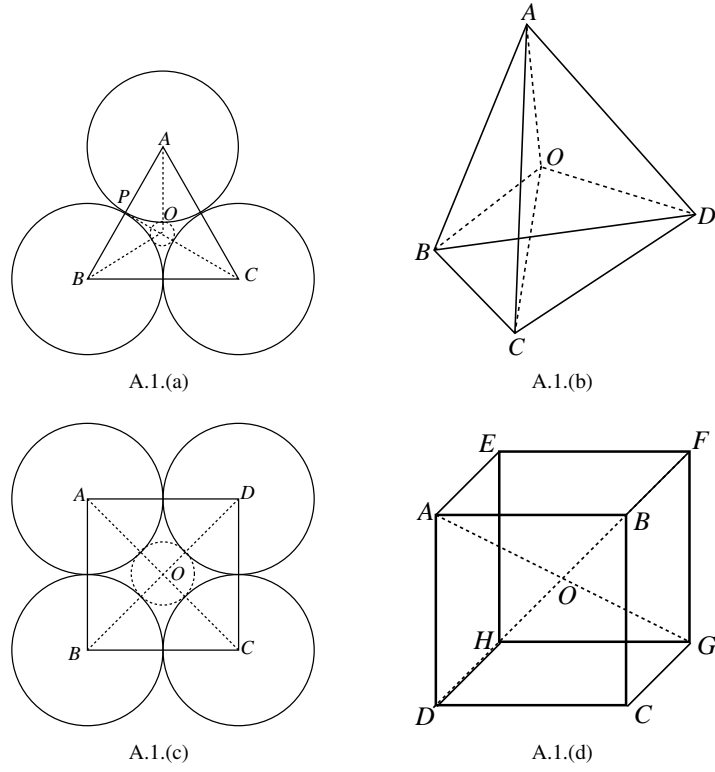
34

A.1.(a)

A.1.(b)

A.1.(c)

A.1.(d)

Figure A.1: (a) Triangular (b) tetrahedron (c) square and (d) cubic lattices, where the small particle of radius r_3, r_6, r_4 and r_8 respectively is residing between bigger particles of radius r_A, just touching them.
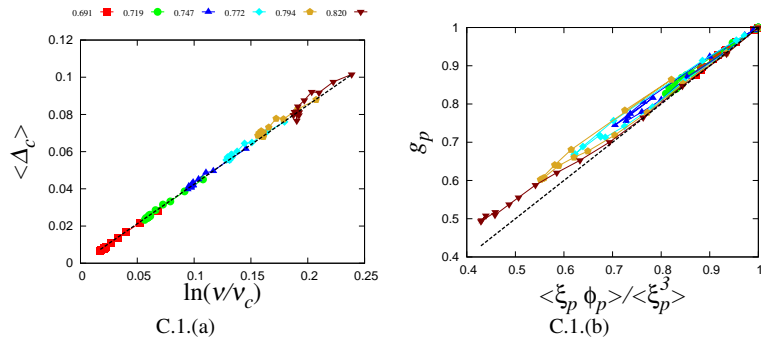

C.1.(a)

C.1.(b)

Figure C.1: (a) $\langle \Delta \rangle_c$ against $\ln(\nu/\nu_c)$ using Eq. (C.8). (b) g_p measured using Eq. (C.10) with the assumption that the total force on a particle is proportional to square of contacts it has with neighbors and is compared with the analytical expression of g_p in Eq. (C.7).